Open Access

Catalysis Research

Review

Perovskite Solar Cells: Assessment of the Materials, Efficiency, and Stability

Binita Boro [1], Shivam Porwal [2], Dinesh Kumar [2], Snehangshu Mishra [2], Subrata Ghosh [2], Sakshi Kansal [2], Amreesh Chandra [3], Trilok Singh [2,*]

1. School of Nano Science and Technology, Indian Institute of Technology Kharagpur, 721302, India; E-Mail: binitaboro47@gmail.com
2. Functional Materials and Device Laboratory, School of Energy Science and Engineering, Indian Institute of Technology Kharagpur, 721302, India; E-Mails: shivam.mst17@gmail.com; 1994dineshbeni@gmail.com; mishra.snehangshu@outlook.com; subrata.subho7@gmail.com; sakshikansal95@gmail.com; trilok@iitkgp.ac.in;
3. Department of Physics, Indian Institute of Technology Kharagpur, 721302, India; E-Mail: achandra.iitkgp@gmail.com

* **Correspondence:** Trilok Singh; E-Mail: trilok@iitkgp.ac.in

Academic Editors: Wei Wang, Simone Mascotto and Bin Lin

Special Issue: Design and Development of Perovskite Materials for Energy Conversion Devices

Catalysis Research
2022, volume 2, issue 4
doi:10.21926/cr.2204033

Received: August 14, 2022
Accepted: September 09, 2022
Published: October 14, 2022

Abstract

Solar cells based on organic-inorganic lead halide perovskites are popular in the photovoltaic community due to their high efficiency, low cost, and solution processability. Understanding the fundamentals of metal halide perovskite and its interfaces is extremely important for achieving high-quality materials and developing efficient devices using these materials with the necessary properties. Various methodologies have been used to evaluate the excellent optoelectronic properties, efficiency, and stability of PSCs. In this article, we reviewed the case studies of characterization techniques to investigate structural, optical, and electrical properties of perovskite material via electron microscopic techniques (SEM and TEM), *J-V* measurements, AFM, XRD, and spectroscopy techniques (PL, UV-vis, XPS, Raman, FTIR, and

EIS). PSCs also need to have long-term stability and large-scale applicability for successful commercialization. In this review, we studied perovskite in detail to understand the key properties of the materials to facilitate the commercialization of PSCs.

Keywords
Perovskite; characterization; stability; PCE

1. Introduction

Halide perovskites have been extensively studied in recent years as a photoactive layer in perovskite-based solar cells. They have a general chemical formula of ABX_3, where A is a monovalent cation (for example, formamidinium, methylammonium, cesium, etc.) located at the center of a cuboctahedral cavity that is surrounded by eight octahedra and coordinated by 12 halide anions. B (Pb^{2+} or Sn^{2+}) is a divalent metal cation that occupies the center of the octahedron, and X (for example, Cl^-, Br^-, and I^-) is a halide anion located at the corner of the BX_6 octahedron [1-4]. By using perovskite as a light absorber in solar cells, the power conversion efficiency (PCE) has increased considerably in just over a decade of its research. Additionally, low cost, ease of fabrication at low temperatures, high absorption coefficients, tunable bandgap, long carrier lifetimes, high charge mobility, and large diffusion length make it better than matured silicon, cadmium telluride (CdTe), and copper indium gallium selenide (CIGS) based solar cell technologies [5-7]. The structure of perovskite solar cell (PSC) devices mainly consists of a transparent conductive oxide (ITO/FTO), an n-type semiconducting electron transport layer (ETL), a perovskite layer, a p-type semiconducting hole transport layer (HTL), a back-contact electrode (Au, Ag, or carbon), with regular n-i-p and inverted p-i-n configurations. In the n-i-p configuration, the ETL is a planar or mesoporous structure where perovskite is sandwiched between an n-type material (TiO_2, [6,6]-phenyl-C_{61}-butyric acid methyl ester (PCBM), etc.) at the bottom and a p-type layer (for example, 2,2',7,7'-Tetrakis [N,N-di(4-methoxyphenyl)amino]-9,9'-spirobifluorene also known as spiro-OMeTAD) at the top, while in the p-i-n configuration, it is the opposite. Each layer plays a significant role in determing the performance and stability of the device [8-10]. The appropriate energy level alignment of perovskite absorbers with their respective ETL and HTL materials ensures efficient collection of the photogenerated carriers [11]. The conduction band of perovskite must be higher than the conduction band of the ETL, whereas the valence band of perovskite must be lower than that of the HTL layer. The energy level diagram of various perovskite absorber layers, ETL, and HTL is shown in Figure 1. Miyasaka et al. used organic-inorganic halide perovskite for the first time in 2009 as a photoactive layer deposited on mesoporous TiO_2 in a photoelectrochemical solar cell and reported a power conversion efficiency (PCE) of approximately 3.8% [12]. After two years, in 2011, Im et al. [13] reported a PCE of 6.54% by ETL/absorber surface treatment. The PCE and stability increased significantly with the same material when the liquid electrolyte in the photoelectrochemical cell was replaced with Spiro-MeOTAD, a solid hole-transporting material [14, 15], achieving a PCE of nearly 10% [16]. Recently, a PCE of 25.7% was achieved [17]. This considerable increase in the PCE was due to the optimization of device architecture, the use of various interface engineering approaches, improvements in the electron and hole transport layers, and the use of various fabrication methods.

Although there are several advantages, PSCs suffer from some limitations that have delayed their commercialization. Among them, long-term instability in a moist environment, degradation caused by ultraviolet (UV) illumination, difficulty in fabrication of large areas devices with full surface coverage uniform perovskite films are of primary concern. The degradation could occur at the grain boundaries or the grain interior due to the effect of various environmental factors, such as light, heat, humidity, etc. [18, 19]. For example, perovskite films may degrade into iodide compounds or by-products when exposed to moisture [20, 21]. Moreover, lead-based perovskites have many limitations due to the toxicity induced by the irreversible degradation of Pb^{2+}. Since lead causes serious health problems in the environment, the commercialization of lead-containing PSCs is of concern. The release of lead into the environment can be minimized by properly encapsulating the PSC device or module. Alternatively, Pb substitutes may be used, such as Sn, Ge, Sb, Bi, etc. However, these substitutes have lower photovoltaic performance than Pb-based perovskite. To match the performance of the alternative metals with a Pb-based device, the alternative metals should possess all the properties that a Pb-based perovskite has. For example, they must have high defect-tolerance to reduce recombination loss, high absorption coefficient, high charge carrier mobility, etc. [22-27]. Sn-based perovskite has similar properties to lead-based perovskite. However, their photovoltaic performance is considerably lower than that of lead-based perovskite. This is due to the oxidation of Sn^{2+} to form Sn^{4+}. Various strategies have been implemented to overcome or suppress the issue of oxidation of Sn^{2+} in Sn-based perovskite. Liao et al. coated a thin layer of phenylethylammonium bromide (PEABr) on $FASnI_3$ perovskite films to improve the interfacial layer between perovskite and the ETL [28]. Inserting PEABr between the $FASnI_3$ film and ETL resulted in good film morphology, suitable energy level alignment, and inhibition of the oxidation of Sn^{2+}. Singh et al. fabricated a lead-free Bi-based perovskite ($(CH_3NH_3)_3Bi_2I_9$) based on a low-temperature solution process using a device with a planar and mesoporous structure and TiO_2 as the ETL [29]. They found that the morphology of the perovskite film strongly depended on the surface on which it was deposited. A perovskite film grown over the anatase TiO_2 layer is more uniform compared to that grown over a compact and brookite TiO_2 layer. Thicker brookite TiO_2 loads lesser perovskite material into it, which prevents uniform film formation. Although the device has a low PCE of 0.2%, it exhibits good stability for up to 10 weeks in the ambient environment. Therefore, Bi-based perovskite is a promising candidate to replace Pb-based perovskite in photovoltaic applications. Two-dimensional perovskites are more stable than three-dimensional perovskites [30-32]. Schlipf et al. investigated the role of low-dimensional perovskites as a humidity barrier in 3D/2D perovskite heterojunctions. The migration of ions in PSCs, which causes current density–voltage (*J*–*V*) hysteresis and a decrease in operational stability, is also a major concern. Tumen-Ulzii et al. introduced an interfacial self-assembled monolayer (SAM) to reduce *J*–*V* hysteresis [33]. They reported that with SAM treatment, almost no degradation in PSCs occurred even under continuous illumination for 1,000 h at room temperature. Therefore, a detailed analysis of perovskite films and the entire device is essential to fully understand the properties of this unique material and its degradation pathways using appropriate characterization techniques [34]. In this study, we analyzed and discussed the properties of perovskite films and materials, including crystal structure, optoelectronic properties, chemical composition, and the overall photovoltaic performance of PSCs. We also discussed various factors that affect the performance and stability of PSCs, along with their mitigation strategies, to facilitate the fabrication of stable perovskite films. This study might assist new researchers in the

field of PSCs in getting an overview of the material properties, various challenges, and different ways to overcome those challenges.

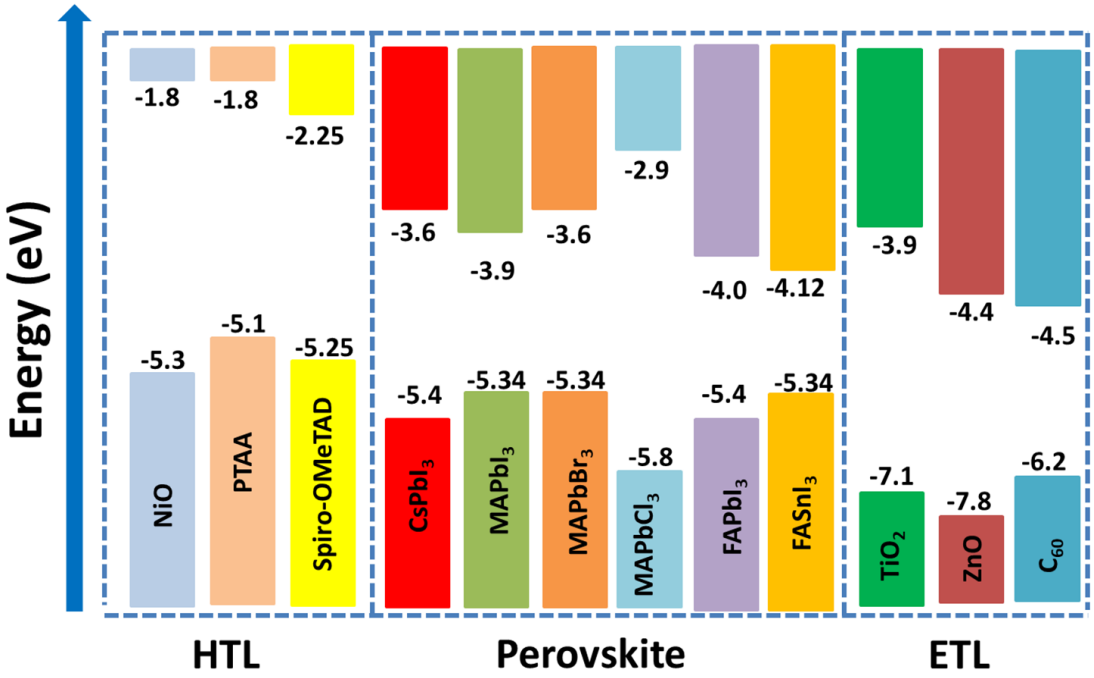

Figure 1 An energy level diagram showing the conduction and valence band of the perovskite absorber, the electron transport layers, and the hole transport layers.

Various microscopic and spectroscopic characterization techniques, such as scanning electron microscopy (SEM), transmission electron microscopy (TEM), X-ray diffraction (XRD), atomic force microscopy (AFM), photoluminescence (PL) spectroscopy, Fourier transform infrared (FTIR) spectroscopy, Raman spectroscopy, Impedance spectroscopy, etc., were used to understand the fundamental properties, for example, perovskite film morphology, grain size, crystallinity, defects, etc., of perovskite films. These characterization techniques might help to understand the effectiveness of various strategies used to optimize the quality of the materials and the properties of the devices to produce stable and inexpensive solar cells.

2. Analysis of the Crystal Structure of Perovskite Films

The structural stability and formability of halide perovskite compounds can be determined by the tolerance factor and octahedral factors and are useful in understanding the structural properties. Moreover, the photovoltaic performance of PSCs depends on the orientation of the crystalline grains, conformation, and dendritic structures. Crystallographic parameters of perovskite materials, such as space group, lattice constant, crystal structure, and the corresponding phase transition temperature, are useful for the structural analysis of perovskite crystals. The organic-inorganic hybrid perovskites undergo phase transition with temperature changes. The X-ray diffraction technique is widely used to determine the crystal structure, chemical composition, electronic structure, and morphology of perovskite. X-ray diffraction can be used to characterize the structural, chemical, and morphological changes during the formation of the perovskite layer and the degradation of perovskite. Combining an X-ray source with an in-situ characterization technique can

also provide information about the stability due to light, the effect of atmospheric conditions, and thermal stress in the perovskite layer [35, 36]. $FAPbI_3$-based perovskite solar cells have become more popular than the traditional perovskite solar cells ($MAPbI_3$) because of the higher thermal stability and more suitable bandgap (1.45 eV) of $FAPbI_3$-based perovskite solar cells. However, the phase stability of α -$FAPbI_3$ (photoactive phase) is a major concern, and the structural transformation from the α-phase to the δ-phase (photo inactive phase) can be traced using in-situ XRD [37-39]. This technique can also be used to characterize the different stages of crystallization of the perovskite layer in each annealing step.

In-situ X-ray diffraction provides the processing phase of the active perovskite layer [40-44] and can help to understand the growth and decomposition mechanism of the perovskite active layer.

Pool et al. performed thermal engineering of $FAPbI_3$ perovskite material using in-situ XRD. They heated the film from 130 °C to 170 °C at a ramp rate of 10°C/s, and they observed three polymorphic transformations of the $FAPbI_3$ film (Figure 2) [37]. During the process, the precursor phase changes in different space groups. It changes from $P6_3$ mC (hexagonal) to P3 m11 (trigonal), which finally leads to the decomposition of the active layer of perovskite. The area under each reflection and the full width at half maximum (FWHM) can be used for the conversion of the phase with temperature and time. Xiao et al. investigated an exfoliated quasi-2D $BA_2MA_2Pb_3I_{10}$ single crystal by performing XRD; all diffraction peaks in the XRD pattern were indexed as (0 k 0) planes of $BA_2MA_2Pb_3I_{10}$. These diffraction peaks were used to analyze the phase structure and orientation of the $BA_2MA_2Pb_3I_{10}$ single crystal [45]. Thus, the XRD technique can be used to effectively perform the phase and orientation analysis of single-crystal perovskite [46, 47].

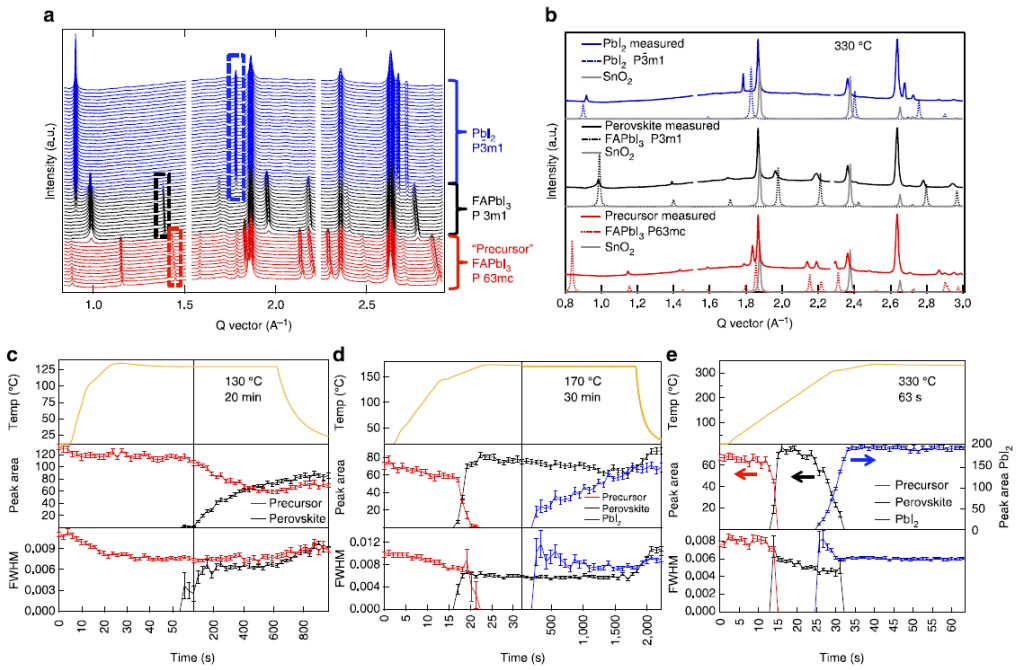

Figure 2 (a) In-situ XRD diffraction of samples was conducted by heating them at 330 °C with phase progression. (b) Phase identification after in-situ XRD was performed from top to bottom; the scans were recorded at 10.7, 16.1, and 42.9 s. (c-e) The integrated intensities of the peaks from the precursor (red lines), perovskite (black lines), and PbI_2 (blue lines) phases are shown as a function of time for films annealed at 130 °C, 170 °C, and 330 °C, respectively [37].

The XRD analysis can also provide information on the time-temperature transformation (TTT) of perovskite films. The different annealing rates facilitate the transformation of the polycrystalline nature of the perovskite thin film. If the full-width at half maximum of the X-ray diffraction peak does not change, the crystallites also remain unchanged. Also, the 'Johnson-Melh-Avrami' [42, 48] model suggests that the different annealing rates do not facilitate the direct transformation from the perovskite layer to PbI_2. The different types of perovskite structures, along with their corresponding crystal structure, space group, lattice constant (Å), and temperature (K), are presented in Table 1.

Table 1 The different types of perovskite structures along with their corresponding crystal structure, space group, lattice constant (Å), and temperature (K).

Structure type	Crystal Structure	Space Group	Lattice Constant (Å)	Temperature (K)	Refs
α-$CH_3NH_3PbI_3$	Cubic	$Pm\bar{3}m$	a = 6.315	350	[49]
α-$CH_3NH_3PbI_3$	Cubic	$Pm\bar{3}m$	a = 6.31728	352	[50]
α-$CH_3NH_3PbI_3$	Cubic	$Pm\bar{3}m$	a = 6.391	338	[51]
α-$CH_3NH_3PbI_3$	Tetragonal (Pseudo-cubic)	P4 mm	a = 6.3115, c = 6.3161	400	[52]
β-$CH_3NH_3PbI_3$	Tetragonal	I4/mcm	a = 8.8796, c = 12.6266	295	[49]
β-$CH_3NH_3PbI_3$	Tetragonal	I4cm	a = 8.849, c = 12.642	293	[52]
β-$CH_3NH_3PbI_3$	Tetragonal	I4/mcm	a = 8.800, c = 12.685	220	[53]
β-$CH_3NH_3PbI_3$	Tetragonal	I4/mcm	a = 8.80625, c = 12.7127	180	[50]
γ-$CH_3NH_3PbI_3$	Orthorhombic	Pnma	a = 8.86574, b = 12.6293, c = 8.57689	100	[50]
γ-$CH_3NH_3PbI_3$	Orthorhombic	Pnma	a = 8.8362, b = 12.5804, c = 8.5551	100	[54]
γ-$CH_3NH_3PbI_3$	Orthorhombic	Pnma	a = 8.8155, b = 12.5980, c = 8.5637	4	[55]
	Cubic	$Pm\bar{3}m$	a = 5.933	298	[51]
	Tetragonal	I4/mcm	a = 8.3381, c = 11.8587	220	[56]
$CH_3NH_3PbBr_3$	Tetragonal	P4/mmm	a = 5.894, c = 5.861	150–155	[57]
	Orthorhombic	$Pna2_1$	a = 7.979, b = 8.580, c = 11.849	<145	[57]

	Cubic	$Pm\bar{3}m$	a = 5.666	200	[51]
$CH_3NH_3PbCl_3$	Tetragonal	P4/mmm	a = 5.656, c = 5.630	173–179	[57]
	Orthorhombic	$P222_1$	a = 5.673, b = 5.628, c = 11.182	<173	[57]
$CH_3NH_3SnI_3$	Tetragonal	I4cm	a = 8.7577, c = 12.429	200	[52]
$CsPbI_3$	Orthorhombic	Pnma	a = 8.856, b = 8.576, c = 12.472	293	[58]
$CsSnI_3$	Cubic	$Pm\bar{3}m$	a = 6.2057	300	[59]
	Tetragonal	P4/mbm	a = 8.7182, c = 6.1908	298	[59]
	Orthorhombic	Pnma	a = 8.68, b = 12.377, c = 8.6384	413	[59]
$CsSnBr_3$	Cubic	$Pm\bar{3}m$	a = 5.80	298	[60]
$CsSnCl_3$	Cubic	$Pm\bar{3}m$	a = 5.604	413	[61]
$CsGeI_3$	Cubic	$Pm\bar{3}m$	a = 6.05	573	[62]
$(CH_3NH_3)_2AgBiBr_6$	Cubic	$Fm\bar{3}m$	a = 11.6370	300	[63]
$(CH_3NH_3)_2KBiCl_6$	Rhombohedral	$R\bar{3}m$	a = 7.8372, c = 20.9938	300	[64]
$Cs_2NaBiCl_6$	Cubic	$Fm\bar{3}m$	a = 10.8429	RT	[65]
$Rb_2LiDyBr_6$	Tetragonal	I4/mmm	a = 7.699, c = 11.032	293	[66]
$(CH_3(CH_2)_3NH_3)_2(CH_3NH_3)_3Pb_4I_{13}$	Orthorhombic	Ama2	a = 8.92, b = 64.383, c = 8.8816	-	[67]
$C_{24}H_{35}S_8N_4PbI_5$	Monoclinic	$P2_1/c$	a = 17.553, b = 8.71, c = 27.122, β = 97.57(2)°	-	[68]
$Cs_3Sb_2I_9$	Hexagonal	$P6_3/mmc$	a = 8.349, c = 20.916	-	[69]

3. Surface Analysis of the Perovskite Film

The performance of perovskite solar cells depends on the morphology, microstructure, surface coverage, and roughness of the surface and the constituent layers, especially the perovskite film. Full surface coverage of the perovskite film (i.e., no pinhole) increases shunt resistance, which prevents current leakage. A smooth surface decreases the defect density and resistance at the interfaces of various layers. Various factors, like defect density, charge diffusion length, and charge dissociation efficiency, depend on the morphology and crystallinity of the perovskite film [7, 70-72].

Thus, various techniques, including modification of the fabrication process, compositional tuning, solvent engineering, additive engineering, and post-fabrication treatment, have been developed to improve the morphology, crystallinity, surface coverage, and interface quality [2, 73-76]. To visualize the changes in morphology, microstructure, and surface coverage of the perovskite film, electron microscopy needs to be performed. Studies on the degradation of perovskite materials induced by various external factors might be conducted by performing electron microscopy. Some additional characterization, such as energy dispersive X-ray spectroscopy (EDS) and electron energy loss spectroscopy (EELS), can also be conducted using a scanning or transmission electron microscope by mounting the needed accessories.

Burschka et al. developed a two-step deposition technique to fabricate the perovskite film on a mesoporous TiO_2 film for controlling the precipitation of perovskite. In contrary, Perovskite films fabricated using single step process results in low surface coverage. In the two-step deposition process, a PbI_2 film is fabricated first, which is expose to CH_3NH_3I solution to convert the film into $CH_3NH_3PbI_3$. The PbI_2 film acts as a template for the perovskite film and regulates the formation of the film. The SEM images showed that the perovskite film fabricated by the two-step process had small grains with full surface coverage, which significantly improved the performance of the device. In contrast, the single-step process produces a perovskite film with large grains but inadequate surface coverage [73]. Singh et al. studied the effect of the concentration of cesium (Cs) and various antisolvents on the morphology of the $Cs_x(FA_{0.83}MA_{0.17})_{(1-x)}Pb(I_{0.83}Br_{0.17})_3$ perovskite film fabricated under air ambient conditions with controlled humidity (RH = 15–25%). The mole fractions of Cs were 0, 0.05, and 0.1 (i.e., x = 0, 0.05, and 0.1; denoted as Cs0, Cs5, and Cs10, respectively). The top-view SEM images showed that the grain growth was the highest, with full surface coverage in Cs5 (Figures 3a-c). The cross-section SEM image showed that the span of one grain covered the total width of the film (Figure 3d). After optimizing the concentration of Cs, they focused on the effects of various antisolvents, including chlorobenzene, ethyl acetate, and toluene. The top view SEM images showed that antisolvent treatment with chlorobenzene led to the highest average grain size (Figures 3e-g) [77]. Large grains improve the charge diffusion length, reduce defects, and enhance the exciton dissociation efficiency, which improves the performance of the device. Plasmonic nanoparticles can be used in perovskite solar cells to increase the absorption and hence, the power conversion efficiency. The interaction between plasmonic nanoparticles and light leads to the absorption and scattering of light [78]. Ali et al. used thermally evaporated plasmonic Ag nanoparticles to improve the performance of perovskite solar cells. The SEM images showed that the nanoparticles were crescent-shaped due to the self-assembly of the Ag atoms at the grain boundaries of the perovskite grains. The size of the nanoparticles depended on the deposition time (0, 100, 300, 500, 700, and 900 s). Deposition for 500 s produced nanoparticles of 79 ±6 nm, which yielded the most efficient perovskite solar cells. The optimized device showed a PCE of 13.46%, which was a 15% increment from the PCE of the control device (PCE of 11.63%) [79].

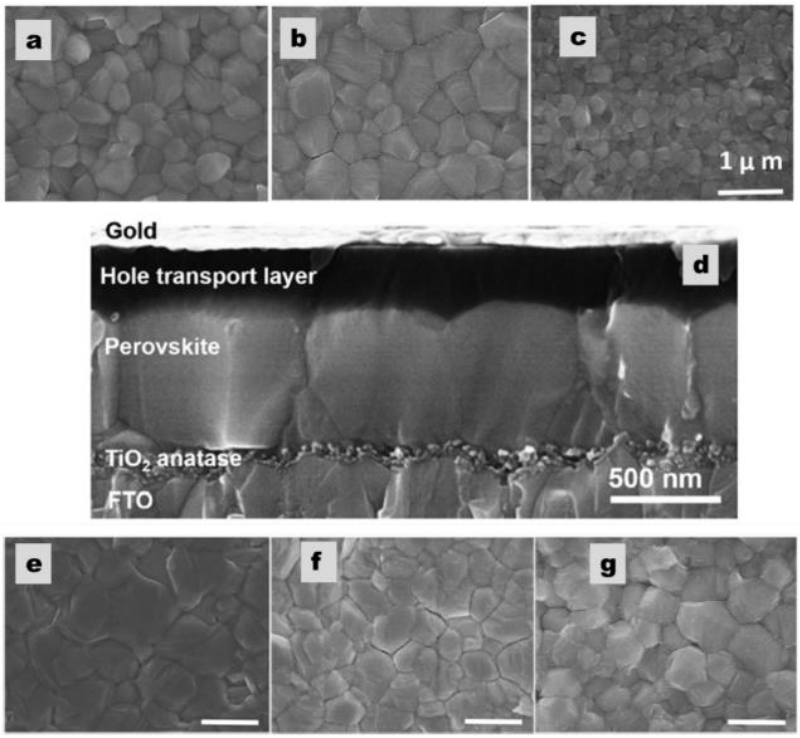

Figure 3 Top views (SEM) of perovskite absorber films prepared from (a) Cs0, (b) Cs5, and (c) Cs10. (d) Cross-sectional view of the perovskite cell (Cs5) with complete device configuration of FTO/TiO_2/meso-TiO_2/perovskite/Spiro-OMeTAD/Au. Top-view SEM images of Cs5 perovskite films with the antisolvent (e) chlorobenzene, (f) ethyl acetate, and (g) toluene dripping; scale bar = 1 µm [77].

Atomic force microscopy (AFM) is another technique to study the morphology of a material. AFM can be used to analyze the surface roughness of perovskite films and various layers within PSCs. Additionally, KPFM and c-AFM can be used to measure the surface potential and determine photovoltaic properties. Aamir et al. investigated the roughness of a cesium lead bromide iodide ($CsPbBr_2I$) perovskite film [80] deposited on a ZnO ETL at different substrate temperatures. The mean roughness was found to decrease with an increase in the substrate temperature (up to 150 °C). Above 150 °C, the film roughness increased because the annealing temperature increased the crystallinity. Yun et al. used AFM on a SnO_2 thin film (ETL) to determine the changes in surface morphology in an annealed film at different temperatures and its effects on the performance of solar cells [81]. They found that the surface of the deposited SnO_2 film was substantially smoother than a bare ITO glass substrate. This indicated that the SnO_2 nanoparticle layers were formed successfully, and the SnO_2 films, which were annealed at 160 °C and 200 °C, created shunting paths by forming pinholes in the SnO_2 ETL. Additionally, scanning probe microscopy (SPM) techniques like Kelvin probe force spectroscopy (KPFM) and conduction force microscopy (c-AFM) can be used to simultaneously identify photovoltaic and structural properties [82-84] by measuring the surface potential of perovskite films and the local photocurrent of perovskite devices, respectively. Using the AFM technique, Kim et al. studied the surface morphology of the $MAPbBr_3$ single crystal. The root mean square (RMS) roughness of the surface was measured and found to be 0.51 nm over a scanning area of 10 × 10 μm^2 using a contact-mode XE-100 AFM (Park Systems). The RMS surface roughness, the average interval of the terrace edge, and the approximate surface off-axis angle of

the $MAPbBr_3$ single crystal were determined. Thus, this technique can be used to effectively analyze the surface of the perovskite single crystal [85]. The increment in the grain size from the pristine sample to the annealed sample leads to a significant change in the fill factor of perovskite devices. It can be characterized using the KPFM technique along with c-AFM, which can be used to determine the local photocurrent, recombination behavior, and carrier transportation. Thus, the optimization and enhancement of the performance of perovskite devices for photovoltaic applications can be estimated using the c-AFM and KPFM characterization techniques. The local dark current [82, 86] in a perovskite device (Figures 4a-d) can be estimated by changing the topography of the active layer of perovskite using c-AFM. The change in the topography from a pristine specimen to an annealed specimen under different conditions of bias is shown in Figures 4e-h.

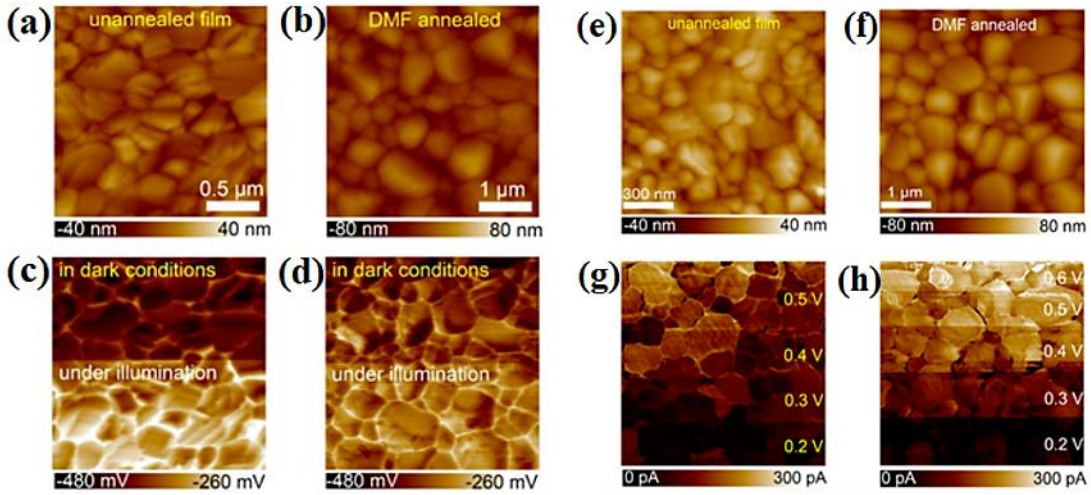

Figure 4 The AFM topographic images of the $CH_3NH_3PbI_3$ perovskite films (a) without and (b) with DMF post-annealing. (c and d) The corresponding CPD distribution of perovskite films under dark conditions (upper half) and illumination (lower half) [87]. The AFM topographic images of the $CH_3NH_3PbI_3$ perovskite films (e) without and (f) with DMF post-annealing. (g and h) The corresponding photocurrent mapping at different bias voltages [87].

4. Compositional Analysis and Degradation Study of Perovskite and Charge Selective Layers

In perovskite solar cells, various materials are used in different constituent layers. To evaluate the composition or detect the presence of a particular dopant or additive and its interactions, Raman spectroscopy, XPS, TEM, and FTIR spectroscopy techniques are used widely. These techniques are also used in degradation studies to detect the decomposed by-products, identify the robust material, or determine the mechanism of degradation. The properties of hybrid perovskites, such as $MAPbI_3$, depend on various types of interactions and structural disorders. The interaction between the organic cation and the halide anion (for example, the NH_3^+ group of the MA cation and the halide atoms in $MAPbX_3$) in perovskite is determined by the hydrogen bonding between them. Detailed knowledge of hydrogen bonding might help in understanding the properties (optoelectronics properties, photovoltaic behavior, stability, etc.) of the perovskite material. Studying the vibrational modes by performing Raman spectroscopy can elucidate the structure of this material and monitor the phase transition behavior of perovskite materials [88]. By analyzing

the Raman peak positions, spectral line widths, and intensities, the composition of the material used in the sample can also be determined. Quarti et al. performed experimental and theoretical studies to assign Raman vibrational spectra of $MAPbI_3$ in the low-frequency region [89]. They assigned bending and stretching vibrational bands of Pb-I bonds at 62 cm^{-1} and 94 cm^{-1}, respectively. The bands at 119 cm^{-1} and 154 cm^{-1} were formed due to the liberation of MA cations. Also, unstructured features at 200–400 cm^{-1} were assigned to the torsional mode of MA cations. Ruan et al. performed Raman spectroscopy of single-crystal metal halide perovskites based on $FAPbX_3$ (X = Cl, Br, and I) and $FA_xMA_{1-x}PbI_3$ and determined the correlation between the perovskite composition and Raman spectra [90]. They found that by tuning the halide content there is a shift in the Raman spectra of the organic characteristics. This occurred due to the changes in the strength of the hydrogen bond. Tuning the organic cation changed the peak intensity (Figures 5a and b). A more intense peak indicated that there was a change in the cation ($FA_xMA_{1-x}PbI_3$ single crystals) perovskite.

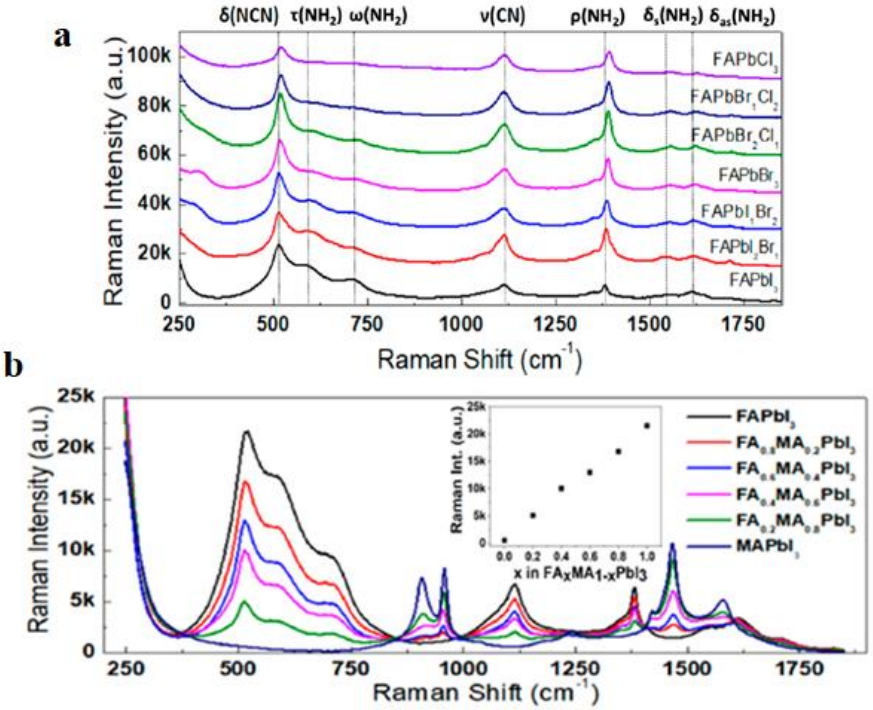

Figure 5 (a) The Raman spectra of $FAPbX_3$ mixed halide perovskite, where δ, τ, ω, ν, and ρ represent bending, torsion, wagging, stretching, and rocking, respectively. (b) The Raman spectra of mixed A-site (Inset) Linear dependence of the Raman intensity at 511–516 cm^{-1} with increasing FA ratio [90].

The Raman peak intensities also depend on the crystallinity of the perovskite material, and this can be used to study the phase transition temperature of perovskites [88]. Kim et al. used PEDOT: PSS remodeled with copper sulfate (CuS) nanoparticles (NPs) as a hole transporting material in inverted perovskite solar cells. They performed Raman spectroscopy to investigate the changes in the molecule and the chemical bond of PEDOT: PSS [91] with different amounts of CuS NPs. They observed a shift in the Raman peak relative to the reference PEDOT: PSS when CuS NPs were introduced. The shift in the Raman peak was attributed to the structural changes in the inner shell bond of PEDOT: PSS from a benzenoid structure to a quinoid structure. The high-intensity laser beam in Raman spectroscopy might lead to the degradation of the perovskite film. Ledinsky et al. reported

structural changes in the $MAPbI_3$ perovskite under a laser illumination at 514.5 nm, where $MAPbI_3$ was converted to PbI_2 [92], whereas laser excitation at 830 nm avoided the formation of PbI_2. They showed that the iodine-to-bromine atom ratio in the mixed halide perovskite layer could be predicted by the shift in the Raman peak. Similarly, Pistor et al. used performed l532 nm and 633 nm laser to detect and monitor the degradation of perovskite solar cells [93]. Excitation at 633 nm was less harmful than excitation at 532 nm. Therefore, while performing Raman spectroscopy of a sample, proper selection of the excitation wavelength is essential.

X-ray photoelectron spectroscopy (XPS) is another promising technique for studying the composition of perovskite materials. Deepa et al. performed XPS to study the triple cation mixed halide perovskites with varying Cs content. They used three perovskites, including $(MA_{0.15}FA_{0.85})Pb(I_{0.85}Br_{0.15})_3$, $Cs_{0.05}(MA_{0.15}FA_{0.85})_{0.95}Pb(I_{0.85}Br_{0.15})_3$, and $Cs_{0.1}(MA_{0.15}FA_{0.85})_{0.9}Pb(I_{0.85}Br_{0.15})_3$, and studied the robustness of these perovskites by Ar^+ sputtering. The XPS spectra showed the presence of Pb^0 (indicating the degradation of perovskite), which was absent before Ar^+ sputtering. The ratio of Pb^0 to Pb^{2+} obtained from the XPS spectra indicated that $Cs_{0.05}(MA_{0.15}FA_{0.85})_{0.95}Pb(I_{0.85}Br_{0.15})_3$ was the best composition, and it retained over 77% structural robustness [94]. Wu et al. used pentaerythritol tetrakis(3-mercaptopropionate), a multi-ligand molecule (denoted as ML), to passivate under coordinated Pb^{2+} and suppress the formation of Pb^0. XPS was performed to confirm the results. The XPS spectra showed that the peak for Pb $4f_{5/2}$ and Pb $4f_{7/2}$ of perovskite had shifted toward lower binding energy after applying the ML, indicating an interaction between uncoordinated Pb^{2+} and the ML. Additionally, the peak for Pb^0 disappeared after applying the ligand. The Pb^0 peak was absent from the perovskite/ML XPS spectra even after five scans. In contrast, the control perovskite XPS spectra showed an increase in the Pb^0 peak with the number of scans (Figures 6a-c). These observations suggested that the ML suppressed the formation of metallic lead [95]. Zhang et al. doped TiO_2 ETL with Mg to enhance the conductivity of the ETL. Sintered TiO_2 ETL was treated with $MgCl_2$ containing a $TiCl_4$ aqueous solution. High-temperature heat treatment (500 °C) was performed for the effective diffusion of Mg ion into the TiO_2 ETL. XPS was performed to confirm that Mg doping was successful. The XPS spectra showed the Mg 1S peak. Moreover, the XPS spectra of the $MgCl_2$-treated TiO_2 showed a Ti $2P_{3/2}$ peak shift (~70 meV) toward higher binding energy. These observations indicated effective Mg doping in the TiO_2 ETL [96]. Das et al. studied the effect of continuous illumination in an open circuit. They applied a voltage under dark conditions and operating conditions on $CH_3NH_3PbI_3$. The XPS spectra showed that a Pb^0 peak appeared under illumination, and the intensity increased over time. In contrast, the peak intensity of Pb^{2+}, N, and I decreased over time. These observations suggested the degradation of $CH_3NH_3PbI_3$ under illumination. The XPS spectra showed that $CH_3NH_3PbI_3$ did not degrade after applying a voltage under dark conditions. This indicated that photogenerated charge carriers might be responsible for the degradation of $CH_3NH_3PbI_3$. A combination of illumination and the applied voltage caused slow degradation of $CH_3NH_3PbI_3$ due to the extraction of photogenerated charge carriers [97]. Single crystals lack grain boundaries, whereas polycrystalline films contain many grain boundaries and irregularities. Hence, halide perovskite single crystals can show better optoelectronic properties than polycrystalline films, such as longer charge carrier diffusion length, low defect density, and suppressed ion migration [98, 99]. However, halide perovskite single crystals may have surface defects due to the re-dissolving of MA cations into the residual solution during fabrication. Song et al. performed a simple MAI surface treatment on the $MAPbI_3$ single crystal to passivate the surface defects and improve the energy level alignment with the anode. In the XPS

spectra, the peak for the metallic lead of the control single crystal was observed, which indicated the presence of defects on the surface. In contrast, the XPS spectra of the MAI-treated single crystals did not show any metallic lead peak, indicating the passivation of surface defects. The MAI surface-treated lateral structure single-crystal PSCs showed a high power conversion efficiency of 11% [100].

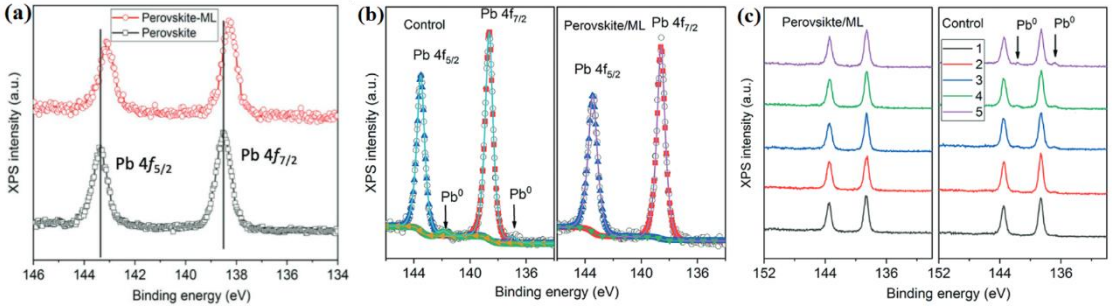

Figure 6 (a) The XPS spectra and comparison of binding energies corresponding to the Pb-4f core level of perovskite and the perovskite-ML complex. (b) The XPS spectra (Al−Kα = 1,486.6 eV) of the Pb-4f core levels of perovskite were derived from the first scan. (c) The evolution of Pb^0 was detected in five consecutive scans by performing XPS [95].

Transmission electron microscopy is another strong tool to determine the degradation pathways of perovskites. Divitini et al. studied the thermal response of $MAPbI_3$ by performing in-situ TEM and found that fabrication methods influence the mechanism of degradation [101]. Yang et al. studied the morphological and structural degradation of methylammonium lead iodide ($MAPbI_3$)-based perovskite solar cells by performing TEM. A comparison of the ex-situ TEM images of freshly prepared samples with those exposed to air for six days showed that phase segregation and degradation occurred in the perovskite layer after exposure to air. Additionally, the results of electron energy loss spectroscopy showed oxygen-rich and iodine-rich portions in degraded perovskite. These findings validated the hypothesis that the presence of oxygen facilitates the degradation of organic cations and leaves iodine-containing by-products. Based on the results of in-situ TEM, a study showed that heat-induced degradation could be accelerated by the defects present in the samples. In contrast, the results of in-situ TEM showed that a high vacuum is not responsible for degradation [102]. Kim et al. conducted an in-situ HRTEM study on the thermal degradation of $MAPbI_3$ and identified trigonal PbI_2 as a degradation by-product. Surprisingly, the precipitation of PbI_2 from the amorphous $MAPbI_3$ layer occurred via an intermediate state [103]. Seo et al. performed a comparative heat-induced degradation study on $MAPbI_3$ and $Cs_x(FA_yMA_{(1-y)})_{(1-x)}Pb(I_zBr_{(1-z)})_3$ using in-situ TEM. They found that MA-based perovskite degraded as the temperature increased and formed particles and voids. At 150 °C, the MA perovskite-based devices failed due to severe degradation. In contrast, MA-FA-Cs-based triple cation perovskite was stable up to 130 °C. At 150 °C, there was some indication of degradation, while severe degradation with particle and void formation was observed at 170 °C. The higher thermal stability of triple cation perovskite is attributed to the presence of inorganic Cs cations, thermally stable (comparatively) FA cations and stronger interaction of FA with PbI_6 [104].

FTIR spectroscopy has been extensively performed using perovskite materials by different research groups to analyze the degradation mechanisms in PSCs. Abdelmageed et al. studied the light-induced structural degradation of $MAPbI_3$ perovskite [105]. No change occurred in the peak

related to the CH_3 group before and after exposure to light (Figure 7a). Only a change in the peak position and intensity of the NH_3 group appeared in the spectra, suggesting that the NH_3 of MA was involved in the degradation due to light. By performing in-situ diffusion-reflectance FTIR spectroscopy, Yu et al. showed that even at a low temperature of 60 °C, $MAPbI_3$ could decompose slowly to form CH_3NH_2 [106]. Similarly, the humidity-induced degradation of ($CH_3NH_3Pb(I_{1-x}Br_x)_3$) perovskite was investigated by Gan et al., where they observed a broad band of –OH vibration around 3,200 cm^{-1} and considerably stronger bands around 1,200–1,700 cm^{-1} appeared after hydration. They concluded that the band at 1,660 cm^{-1} might be used as a reference peak for determining the degree of hydration in mixed halide perovskites [107]. The method used to synthesize PSCs also decides the performance and stability of the device. Venkatesan et al. discussed the need for a humid environment to develop a high-quality perovskite film [108]. They found that exposing a perovskite film to ambient air before thermal annealing increased the PCE. The FTIR spectra of the resultant film showed that the moisture in the air enhanced the formation of the perovskite film. Dhmaniya et al. studied the degradation of perovskite films fabricated in three different ways (single-step with lead chloride precursor, single-step with lead acetate precursor, and a two-step process) [109]. The FTIR spectra of perovskite films fabricated using three different methods are shown in Figures 7b-d. The peaks around 1,420–1,463 cm^{-1} were due to C–H bending, those around 1,575–1,650 cm^{-1} were due to N–H bending, and the peaks around 3,100–3,200 cm^{-1} were due to N–H stretching. A broad shoulder around 3,450–3,550 cm^{-1} was due to the hydrogen bonding in the lead chloride-based device. A strong and broad vibration was observed around 3,100–3,500 cm^{-1} for the same. However, no such peaks were observed for the two-step and lead acetate-based devices. This suggested that in the lead chloride-based device, the perovskite interacts with water through hydrogen bonding to form an intermediate hydrate. Furthermore, ion migration-induced degradation in halide perovskite leads to instability in the performance of the device [110, 111]. Suppression of ion migration can minimize the defects in the perovskite. In a study, polycaprolactone (PCL), a polar polymer, was added to $MAPbI_3$ perovskites to suppress ion migration by passivating the grain boundaries [112]. A shift in the C =O stretching peak of PCL to a higher wavenumber from 1,720 cm^{-1} to 1,725 cm^{-1} in PCL-incorporated $MAPbI_3$ showed the interaction between PCL and $MAPbI_3$. The redshift of C =O stretching vibration from 1,720 cm^{-1} to 1,728 cm^{-1} in PCL-incorporated PbI_2 indicated that PbI_2 of $MAPbI_3$ interacts with the PCL. Similarly, Zheng et al. fabricated a $CH_3NH_3PbI_3$ perovskite film co-crystallized with poly(ethylene oxide) (PEO) using a single-step process to suppress ion migration and reduce photocurrent hysteresis in PSC. They performed attenuated total reflectance FTIR spectroscopy to confirm the formation of a hydrogen bond between poly(ethylene oxide) and $CH_3NH_3^+$ in a PEO-added $CH_3NH_3PbI_3$ perovskite film. Weaker and broader O–H stretching vibration in the PEO-$CH_3NH_3PbI_3$ solution than that in the PEO solution and diminished N–H stretching band at approximately 3,250 cm^{-1} confirmed the interaction between PEO and the perovskite. Such hydrogen bonding can minimize ion migration and reduce defects in perovskite films [113]. Trap states formed on the surface of the perovskite film and at grain boundaries during the fabrication of the perovskite film restrict the performance and stability of PSCs. These trap states act as recombination centers for the charge carriers. They also promote the entry of oxygen and moisture into the perovskite film, thus, significantly affecting the stability of the device. Therefore, fewer defect states can enhance the performance and stability of the device. Passivation methodology, including additive engineering, interface engineering, and antisolvent engineering, significantly increase the stability and the PCE of PSCs. Passivating the

perovskite film results in the formation of a hydrophobic film with few defects, good crystallinity, and large grain size. Various research groups have performed FTIR spectroscopy to investigate different solvents, anti-solvents, and additives used during perovskite deposition [114-118]. For example, Garai et al. used poly(p-phenylene)-based conjugated polyelectrolytes PHIA functionalized on the side chain to efficiently passivate the trap states in perovskite films [119]. The negative charge in the carboxylate ion side chain of PHIA can passivate the positively charged defects in perovskite films. This was confirmed by the shift of the FTIR spectrum of the carboxylate ion of PHIA from 1,705 to 1,642 cm^{-1}, which indicated the interaction of the carboxylate ion with the perovskite, and thus, the efficient passivation of the perovskite film. Using this passivation strategy, they obtained a highly stable device due to an increase in the hydrophobicity of the perovskite film. Kim et al. post-treated a $FA_{0.9}Cs_{0.1}PbI_{2.8}Br_{0.2}$-based perovskite film with different concentrations of pyridinium iodide (PyI) and piperidinium iodide (PpI) (5, 20, and 40 mM) [120]. They found that the PCE of PyI-based devices gradually increased with an increase in the concentration of PyI. However, the performance of the device decreased as the PpI concentration increased. Based on the results of the XRD, the authors reported the formation of a 1-D $PpPbI_3$ layer between the perovskite and the HTL, which could block charge separation in case of a PpI post-treated device with higher PpI concentrations. This was further confirmed by performing FTIR spectroscopy, where PpI was found to interact more strongly with PbI_2 than PyI, which supported the formation of a 1-D $PpPbI_3$ layer post-treatment as the concentration of PpI increased. Han et al. used polypropylene carbonate (a polymeric Lewis base) to passivate the defect formed at the grain boundaries of polycrystalline perovskite films. They performed FTIR spectroscopy to study the interaction between perovskite precursors and Lewis bases [121]. When a Lewis base of higher dipole moment than DMSO (e.g., poly(propylene carbonate)) was added to perovskite precursors, $CH_3NH_3I.PbI_2$.DMSO.Lewis base adduct was formed. A peak related to N–H stretching shifted to a higher wavenumber after adduct formation. Additionally, the peak related to C =O stretching due to poly(propylene carbonate) (PPC) redshifted from 1,760 cm^{-1} to 1,743 cm^{-1}. The shift to a lower wavenumber showed a weakening of the bond strength between carbon and oxygen. This occurred due to adduct formation, suggesting a strong interaction between NH_3^+ and oxygen of PPC. The formation of the intermediate adduct resulted in the formation of a highly crystalline and environmentally stable perovskite film with passivated grain boundaries. Troughton et al. investigated the FTIR spectra of toluene and ethyl acetate, used as an anti-solvent for perovskite precursors containing different quantities of water [122]. They observed a deepening of the ethyl acetate peak at 3,650 cm^{-1} with an increase in the water content, which indicated the ability of ethyl acetate to absorb water. In contrast, toluene can dissolve less, water, indicating toluene's inability to absorb water from moist air less effectively than ethyl acetate.

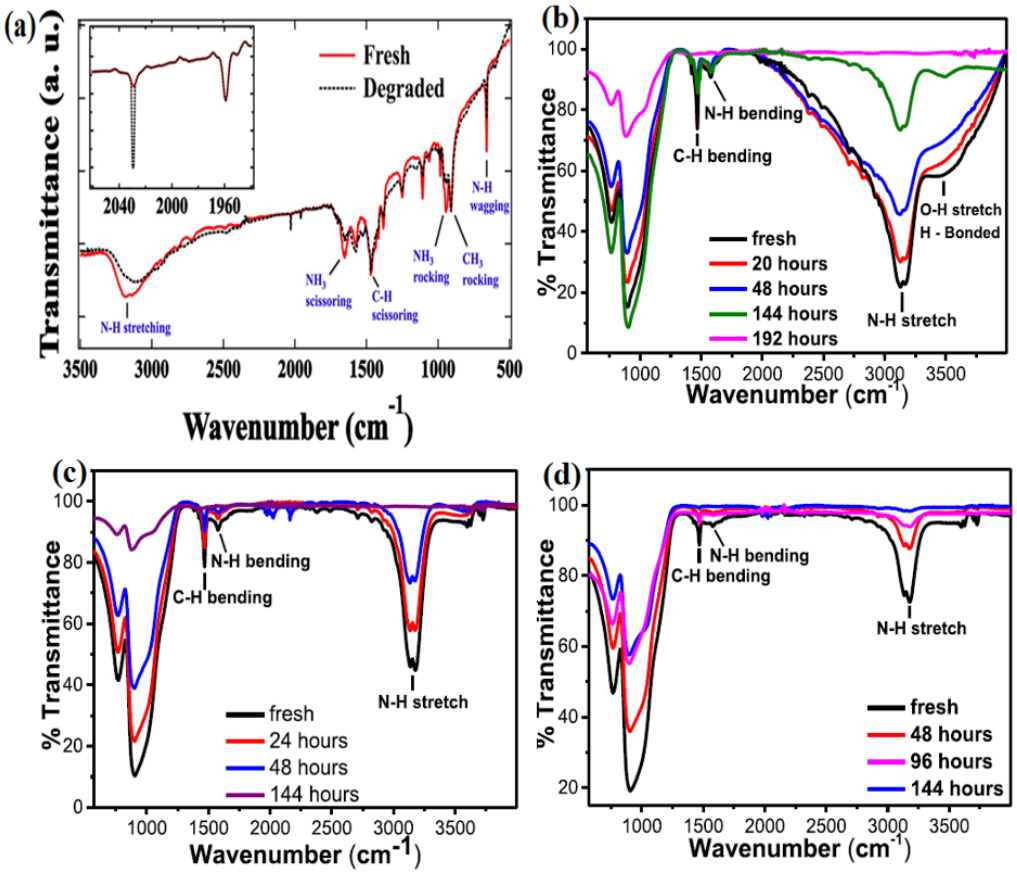

Figure 7 (a) The FTIR spectra of light-induced degradation of $MAPbI_3$ film in dry air; the inset shows changes in the C–O stretching mode at 2,030 cm^{-1} after degradation [105]. The FTIR spectra of a film synthesized using (b) single-step lead chloride as the precursor (c) a two-step process, and (d) single-step lead acetate as the precursor [109].

The intermediate phase formed during the synthesis of perovskite is a critical step for producing uniform crystalline perovskite films. The chemical composition of the intermediate phase (PbI_2-MAI-DMF) formed during the synthesis of a perovskite film was investigated in detail by Guo et al. [123]. The C =O stretching vibration for the PbI_2-MAI-DMF intermediate complex appeared between the DMF and PbI_2-DMF stretching vibration. The interaction between MA^+ and Pb^{2+} facilitated the weakening of the C =O bond strength of the PbI_2-MAI-DMF intermediate phase. The disappearance of the C =O bond from DMF and the redshift of the N–H band to a lower wavenumber after perovskite formation suggested a stronger interaction with the inorganic part in the compact $MAPbI_3$ perovskite lattice. Similarly, Jeon et al. investigated the intermediate phase (CH_3NH_3I-PbI_2-DMSO) formed by the solution-processed $CH_3NH_3Pb(I_{1-x}Br_x)_3$ perovskite, using gammabutyrolactone and DMSO as a solvent followed by toluene drop-casting [124]. FTIR spectroscopy was performed to determine the presence of MAI and DMSO in the PbI_2 layer. The presence of both N–H and S–O stretching modes in the intermediate phase confirmed the incorporation of MAI and DMSO in the PbI_2 layer. In contrast, the C =O modes, which were due to toluene dripping, were not observed in the FTIR spectra. Zhang et al. studied the formation of MAI-PbI_2-DMSO in the intermediate phase when ethyl acetate was added to a spin-coated perovskite precursor [125]. The S =O stretching vibration related to PbI_2-DMSO and MAI-PbI_2-DMSO had a lower wavenumber than DMSO, and the S =O stretching vibration for MAI-PbI_2-DMSO was lower than that for PbI_2-DMSO. Based on Hook's

Law, for a diatomic molecule, the frequency of vibration is proportional to the force constant. Thus, a decrease in the S =O stretching frequency indicated a decrease in the force constant, which was due to a decrease in the strength of the bond between sulfur and oxygen after adduct formation. Similarly, Ahn et al. observed a shift in the S =O stretching vibration to a lower wavenumber for MAI-PbI_2-DMSO compared to that for pure DMSO and PbI_2-DMSO for a perovskite film fabricated using a Lewis Base adduct of PbI_2 (Figures 8a and 8b) [126]. They also concluded that the decrease in the S =O stretching frequency occurred due to a decrease in the force constant as a result of a decrease in the bond strength between sulfur and oxygen after adduct formation. FTIR spectroscopy was also performed to analyze the composition of the intermediate phase formed when the perovskite precursor complex (PbI_2-MAI) was exposed to DMSO and DMF vapors for a few seconds before undergoing thermal annealing [127]. For the DMSO-exposed intermediate phase, a peak at 1,017 cm^{-1} was observed in the FTIR spectra. This peak was attributed to the S =O vibrations, which confirmed the presence of DMSO in the intermediate phase. However, no peak corresponding to DMF was found for the DMF-exposed film. This suggested that the intermediate phase formed after exposure to DMF did not contain DMF.

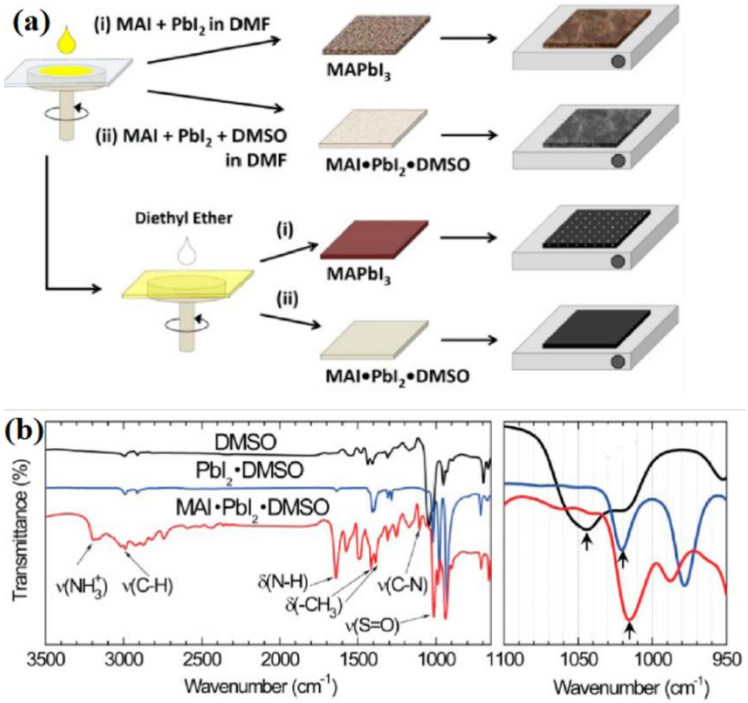

Figure 8 (a) Schematic representation of the fabrication procedure and the plane view scanning electron microscopy (SEM) images of the $MAPbI_3$ perovskite layers obtained by the direct one-step spin-coating of the DMF solution containing MAI and PbI_2 or MAI, PbI_2, and DMSO and diethyl ether dripped while spinning the film. (b) The FTIR spectra of the DMSO solution, PbI_2·DMSO powder, and MAI·PbI_2·DMSO powder; zoomed image of the fingerprint region corresponding to the S =O vibrations [126].

The interaction between the perovskite absorber layer and selective contacts helps to obtain a stable hysteresis-free device. Tirado et al. used nickel oxide (NiO_x) nanocrystals (NCs) as an HTL in $(FAPbI_3)_{0.78}(MAPbBr_3)_{0.14}(CsPbI_3)_{0.08}$ (CsFAMAPbIBr)-based triple cation n-i-p PSCs [128]. They synthesized hydrophilic and hydrophobic NiO_x NCs. The hydrophobic NCs were prepared through

the ligand exchange method using a concentrated oleylamine solution in chlorobenzene. FTIR spectroscopy was performed to confirm the exchange of ligands. The hydrophilic NCs showed an absorption peak at 1,336 cm^{-1} due to the presence of nitrate ions, a broad band at 3,350–3,400 cm^{-1}, and a sharp band at 1,630 cm^{-1} due to the adsorption of water on the surface. However, sharp peaks related to $-CH_2$ and $-NH_2$ scissoring at 1,400 and 1,533 cm^{-1}, respectively, were observed in hydrophobic NCs. Also, the appearance of peaks related to symmetric and antisymmetric C–H stretching vibrations confirmed the presence of aliphatic amines on the surface of the NCs. The hydrophobic NiO_x NCs formed stable colloidal dispersion in nonpolar solvents and were compatible with perovskite. Thus, they can be used as an inexpensive stable HTL in n-i-p structured PSCs. FTIR spectroscopy is a powerful technique for understanding the interaction between the organic and inorganic parts of halide perovskite solar cells. The interaction between various layers of perovskite solar cells and their effectiveness can also be studied using this technique. FTIR spectroscopy is also a powerful technique to study the mechanism of degradation of perovskite solar cells due to various factors that lead to the instability of the devices. This technique was also used in many studies to elucidate the effects of various solvents, additives, etc., used for fabricating perovskite films [115]. The different types of vibrations and vibrational ranges shown by perovskite compounds, obtained from various studies, are summarized in Table 2.

Table 2 Different types of vibrations and vibrational ranges of perovskite, hole transporting materials, solvents, and intermediate compounds formed during perovskite fabrication were determined by performing FTIR spectroscopy.

Compounds	Types of Vibrations	Vibrational Range (cm^{-1})	Remarks	Refs
$MAPbI_3$	C–H bending	1420–1463 cm^{-1}, 1419–1463 cm^{-1}		[109] [129]
	N–H bending	1575–1650 cm^{-1}, 1571 cm^{-1}	Associated with the NH_3^+ group of the MA cation	[109]
		1556 cm^{-1}		[129]
	N–H stretching	3100–3200 cm^{-1}, 3088 cm^{-1}	Associated with the NH_3^+ group of the MA cation	[123] [109]
	C–H stretching	3162 and 3250 cm^{-1}, 2920 cm^{-1}	Asymmetric C–H stretching vibrations	[129] [113]

		2975 cm^{-1}, 2932 cm^{-1}	Symmetric C–H stretching vibrations	[129] [130]
DMSO	S =O stretching	1045 cm^{-1}	Red shifted after adduct formation due to decrease in bond strength between S =O	[125] [126]
PbI_2.DMSO Powder	S =O stretching	1022 cm^{-1}, 1020 cm^{-1}		[124] [127]
MAI.PbI_2.DMSO Adduct	S =O stretching	1018 cm^{-1}, 1015 cm^{-1}		[124] [127]
DMF	C =O stretching	1665 cm^{-1}		[123]
PbI_2.DMF	C =O stretching	1614 cm^{-1}	Red shift	[123]
PbI_2.DMF.$MAPbI_3$	C =O stretching	1631 cm^{-1}		[123]
P3TAA	C–H stretching C–O stretching	2922 cm^{-1}, 1168 cm^{-1}		[129]
$MAPbI_3$/P3TAA	N–H stretching	3126 cm^{-1}		[129]
$MAPb_{(1-x)}Sn_xCl_3$ (x = 0%, 0.5%, 2.5%, 10%, 20%, 33%)	C–Cl stretching	810–910 cm^{-1}	Strong peak	[131]
	C–N stretching	1188 cm^{-1}	Weak peak	
	CH_3-NH_3^+ bending	1458 cm^{-1}	Strong peak	
	N–H bending	1576 cm^{-1}	Weak peak	
	NH_3^+ stretching	3126 cm^{-1}	Broad peak	
		540–590 cm^{-1}	Broad peak (Sn particle)	

5. Optoelectronic Properties of Perovskite Film

Various spectroscopic analyses have been performed to characterize solar cells, including perovskite solar cells (PSCs), to better understand the optoelectronic properties of semiconducting materials. UV-visible spectrophotometers are extremely useful for developing solar cells as they measure the optical properties, such as absorbance and transmittance of semiconducting materials [132].

5.1 Bandgap Analysis of Perovskite Films

By tuning the halide content and the cations in the perovskite, the bandgap can be varied to enhance the efficiency of PSCs depending upon their operation [82]. The optical band gap derived from the UV-Visible spectrum (with the help of Tauc's plot) of the semiconducting material should

match the solar spectrum range (1.1–1.5 eV) to obtain PSCs with good efficiency [133]. Kulkarni et al. used the sequential deposition method for band gap tuning of mixed halide perovskites ($MAPb(I_{1-x}Br_x)_2$ ($0 \leq x \leq 1$)) [134]. They dipped the PbI_2 films in a mixture of MAI and MABr with different molar concentrations of the precursor solutions. With an increase in the MABr content in the mixture, the absorbance band in the UV-Visible spectra shifted toward the lower wavelength region, as shown in Figure 9a, and the band gap increased from 1.56 eV (for pure iodide perovskites) to 2.23 eV (for bromide-rich perovskites). Based on the absorbance data from in-situ UV-Visible measurements, the synthesis of the perovskite absorber layer can be monitored. Unger et al. used lead chloride and methylammonium iodide precursors for perovskite film formation and monitored the formation of the $MAPbCl_xI_{3-x}$ film with a fiber optic UV-Visible spectrometer during annealing [36]. The absorption below 740 nm increased continuously for the first 30 min, and then, the absorption spectrum remained unchanged for the rest of the annealing period. The continuously increasing absorption indicated the growth of the $MAPbCl_xI_{3-x}$ film, whereas the constant absorption suggested that the synthesis of the film formation was completed. Similarly, Hu et al. studied the laminar air-knife-assisted drying kinetics based on in-situ UV-Visible measurements [135]. Based on the time-resolved absorption spectra, they divided the drying process into three stages, including no absorbance, increasing absorbance, and stabilized absorbance. These stages correspond to the nucleation and crystal growth process via solvent evaporation. Several studies have investigated the optoelectronic properties of perovskite single crystals extensively for photovoltaic applications [136]. Perovskite nanocrystals (NCs) are also applied for PSC fabrication owing to the unique properties of the NCs, such as bandgap tunability and solution processability. Studies on UV-visible absorption spectra and bandgap can help to analyze the optoelectronic properties of the NC film effectively when the amount of surface ligands is varied to tune the properties. For controlling the number of ligands around the NC, Liu et al. performed a facile hexane/ethyl acetate (MeOAc) solvent treatment method one, two, and three times for which the calculated ligand content was 2.35%, 1.87%, and 1.01%, respectively [137]. When the ligand amount decreased, the UV-visible optical absorbance spectra showed a redshift of the absorption peak. This indicated that the growth of the NCs became easier as the ligand amount decreased. The absorption spectra also showed better light absorption intensity with the the decreased ligand amounts and reflected better device performance as the J_{SC} increased. In-situ absorption spectroscopy can also be performed to study the degradation of perovskites. Yang et al. investigated the degradation of $MAPbI_3$ under conditions of controlled humidity by performing UV-vis spectroscopy [138]. The absorbance data recorded at 98 ±2% relative humidity showed diminishing absorption features at 760 nm and instantaneous bleaching at 500 nm. The associated increase in the background absorbance ($\lambda > 800$ nm) indicated the formation of the large crystallite due to the decomposition of $MAPbI_3$. The change in the absorbance was the greatest at 410 nm, and the change in normalized absorbance occurred over time. The $\tau_{1/2}$ indicates the time when half of the normalized absorbance is observed, and it was around 4 h at 98% relative humidity (RH), whereas $\tau_{1/2}$ was around 34 h at 40% RH. Additionally, the perovskite film stored in a constant dry airflow environment over two weeks showed no change in the absorption spectrum, indicating that the degradation of perovskite films is primarily caused by the moisture in the ambient air, whereas oxygen has a negligible effect.

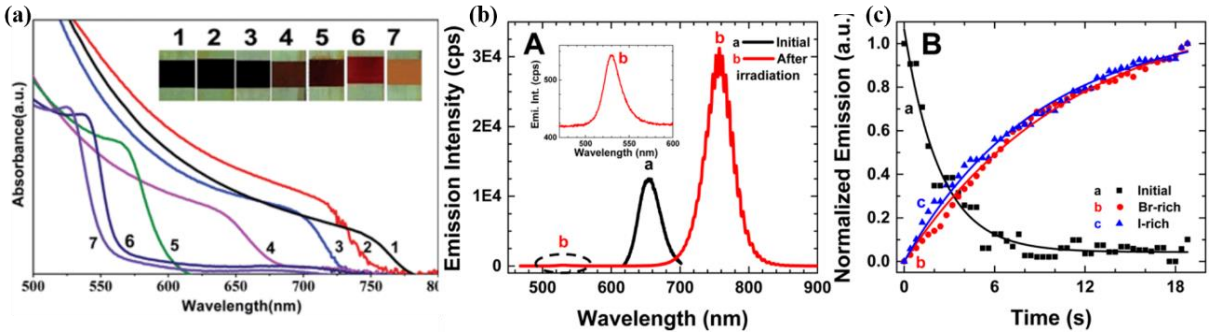

Figure 9 (a) The UV-Vis absorption spectra of the mixed halide lead perovskite ($MAPb(I_{1-x}Br_x)_3$ ($0 \le x \le 1$)) films prepared using the sequential deposition process. Photographs 1 to 7 depict the change in the color of perovskite films on FTO substrates from dark brown/black to orange with increasing bromide content (1 corresponds to the pure iodide-based perovskite film and 7 corresponds to the perovskite film with the highest bromide content) [134]. (b) Emission spectra of a $CH_3NH_3PbBr_xI_{3-x}$ film showing the initial spectrum and the spectrum after 1 min of laser irradiation (405 nm CW laser, 200 mW/cm^2). The enhanced scale of spectrum b in the 400–600 nm region is shown in the inset. (c) Emission changes probed at 655, 530, and 755 nm for the initial $CH_3NH_3PbBr_xI_{3-x}$ film, the Br-rich region, and the I-rich region, respectively [139].

5.2 Carrier Dynamics in Perovskite Films

Several physical processes, such as the transfer of electrons and hole charge carriers, recombination of electron-hole pairs or free carriers, extraction of carriers at the interfacial contacts, and other ionic movements, occur in PSCs within almost similar time domains. These can be detected and analyzed by performing PL and Impedance spectroscopy (IS). The charge carrier lifetime in PSCs is measured via PL decay dynamics obtained from time-resolved photoluminescence (TRPL) measurements [140-143]. Stranks et al. calculated the carrier lifetime and electron-hole diffusion lengths from the TRPL decay curve. For a mixed halide ($CH_3NH_3PbI_{3-x}Cl_x$) perovskite absorber, they obtained long diffusion lengths (>1 µm) for electrons and holes [6]. Similarly, using steady-state PL, Eperon et al. found that PCBM and Spiro-OMeTAD were effective electron and hole transport layers, respectively, and using TRPL, the effective diffusion lengths for electrons and holes were estimated to be approximately 177 nm and 813 nm, respectively [144]. Wang et al. observed a strong PL quenching when perylenediimide dimer (2FBT2FPDI) as a passivating interlayer was incorporated between $MAPbI_3$ and the PCBM. They concluded that the use of 2FBT2FPDI on PCBM-based PSCs can effectively enhance electron transport [145]. By performing photoluminescence spectroscopy, Hoke et al. studied the segregation of halide ions under the visible light-soaking condition in a mixed I/Br perovskite absorber [146], and the phenomenon is popularly known as the Hoke effect. Besides bromide-rich majority domains, lower bandgap iodide-rich minority domains are created upon photo-excitation and later act as “trap” states. However, these light-induced structural changes are reversible. Yoon et al. examined the changes in the emission of a $CH_3NH_3PbBr_xI_{3-x}$ film before and after photo-irradiation based on PL measurements [139]. They showed a weak emission band at 530 nm attributed to the bromide-rich domains and a prominent emission band at 755 nm for the iodide-rich domains (Figures 9b and 9c). Various studies related to halide segregation in mixed-halide perovskites were conducted using the PL technique [147-149].

In a study, deQuilettes et al. combined confocal fluorescence microscopy and time-of-flight secondary-ion-mass spectrometry to study light-induced ion migration in the $CH_3NH_3PbI_3$ perovskite [150]. A significant increase was observed in the PL intensity and the lifetime under illumination, which indicated a decrease in bulk trap state density and migration of iodine away from the illuminated area. The enhancement of Photoluminescence Quantum Yields (PLQY) after surface passivation of the defect sites on the perovskite film ensures better efficiency and stability of PSCs. Ahmed et al. performed dual-surface passivation using YCl_3 to mitigate the surface trap states of the $CsPbCl_3$ perovskite nanocrystals and observed enhancement of PLQY up to 60% while maintaining the crystal size, shape, and structure [151]. Kim et al. studied the surface passivation effect of a melaminium iodide additive on the $(FAPbI_3)_{0.875}(CsPbBr_3)_{0.125}$ perovskite film by steady-state PL and TRPL measurements [152]. The steady-state PL intensity increased after adding melaminium iodide, although the PL peak position did not shift, which implied no change in the bandgap and an increase in the radiative recombination. In the TRPL spectra, the amplitude of the fast decay component (τ_1), related to the non-radiative component, decreased, whereas the amplitude of the slow decay component (τ_2), related to the radiative component, increased as the additive was applied. The carrier lifetime also increased from 460.38 ns for the pristine film to 706.28 ns for the film with the melaminium additive. The additive reduced the non-radiative component but increased the radiative component and, thus, enhanced the photovoltaic performance of the PSC. The PL and TRPL measurements of different perovskite films under various conditions are illustrated in Table 3.

Table 3 The PL and TRPL measurements of perovskite films under various conditions.

Measurement technique	Excitation Source Wavelength	Sample	Remarks	Refs
TRPL	507 nm pulsed excitation	$CH_3NH_3PbI_{3-x}Cl_x$ films with and without thiophene and pyridine treatment	PL lifetime of the perovskite films largely increased (340.7 ±1.1 ns, 2016.5 ±5.3 ns, and 2234.2 ±4.2 ns for the untreated, pyridine treated, and thiophene treated films, respectively)	[153]
Time dependent PL	500 nm	$CH_3NH_3PbI_{3-x}Cl_x$	PL intensity increased under continuous light illumination due to the reduction of the density of bulk defects	[154]
Steady state PL	400 nm	$CH_3NH_3PbI_{3-x}Cl_x$/fulleropyrrolidine with a triethylene glycol monoethyl ether side chain (PTEG-1) and$CH_3NH_3PbI_{3-x}Cl_x$/PCBM	For same illumination time, PL intensity increased largely for perovskite/PCBM samples whereas perovskite/PTEG-1presented less increment	[155]
PL imaging technique	635 nm	c-TiO_2/$CH_3NH_3PbI_3$	Light induced degradation at the c-TiO_2/$CH_3NH_3PbI_3$ interface observed	[156]

			by spatially resolved luminescence imaging	
TRPL	470 nm	$CH_3NH_3PbI_3$	Under low intensity continuous illumination, PL dynamics is dependent on the density of the defect states in the perovskite and hence it is fabrication dependent	[157]
In-situ PL and TRPL	470 nm	glass/FTO/c-TiO2/mp-TiO_2/$CH_3NH_3PbI_3$/spiro-MeOTAD/Au	Under light-soaking condition, initially, the concentration of pre-accumulated positive ions at perovskite/spiro-MeOTAD interface reduces and thereby device performance improves	[158]

Electrochemical impedance spectroscopy (EIS) is used to examine the different electronic/ionic processes that occur simultaneously in PSCs. By analyzing equivalent circuits accurately and fitting Nyquist plots, the internal charge transport dynamics and recombination characteristics of the device can be studied simultaneously.

The illumination of a solar cell greatly influences various processes that occur in it. For example, light irradiation affects the generation and kinetics of charge carriers [159, 160] and their conductivity [99]. Therefore, the charge dynamics and recombination rates are different for a particular device under illumination and in dark conditions. Hence, determining the electrochemical impedance spectroscopy response under different intensities of light irradiation is necessary. Bisquert et al. investigated various studies on the influence of light intensity on the impedance behavior of different types of solar cells [161-164]. In several research articles, the authors discussed the dependence of resistive and capacitive responses of various types of perovskite solar cells at different values of illumination intensities [165, 166]. In most of their articles, impedance spectroscopy [167] was performed under two different voltage conditions, including (i) open-circuit voltage (V_{oc}) and (ii) short circuit or zero bias. The most common results deduced from their studies are as follows: (a) the series resistance (R_s) remains constant with the change in the illumination intensity, as it depends on the Fermi level position, which is fixed for a particular applied bias.

Impedance spectroscopy can be performed to estimate the capacitance in multilayer solar cell devices. There are major capacitive components commonly found in solar cell devices as follows: (a) series resistance (R_s), which remains constant with the change in the illumination intensity as it depends on the Fermi level position, which is fixed for a particular applied bias and found both at open and short circuit voltages. (b) Geometric capacitance (C_g), which dominates in higher frequency (>1 kHz) [167], remains almost unchanged with an increase in the light intensity because it depends on the dielectric constant and thickness of the perovskite layer that is usually kept constant. Finally, (c) accumulation capacitance (C_s), which is prominent in a low-frequency regime (~1 Hz), increases with an increase in the irradiation intensity due to the accumulation of light-induced holes [168], close to the cathode, i.e., the TiO_2 and perovskite layer. Studies on the impedance analysis of the surface recombination process in PSCs [165, 169-171] have shown that the resistive component, i.e., the R_{rec} corresponding to the recombination charge carriers, follows the same trend with an increase in the illumination intensity, with greater values at higher levels of

irradiation. Under certain conditions of illumination, as the light intensity increases, the energy gained by photo-induced electrons also increases, and the charge extraction rate becomes faster, thus reducing the recombination process. In the dark, as there are no photogenerated charge carriers, recombination occurs between the contact materials in the PSC layer; this process takes a long time in most cases. Many studies have performed EIS to assess solar cells under dark conditions [162, 172]. The resistances at the open-circuit voltage were found to have lower values than those in short circuits. In an open circuit, the presence of recombination current almost cancels the photo-induced current, which reduces the resistance. Several studies have also investigated the surface modification of the perovskite layer, the introduction of an interfacial layer other than the ETL/HTL in the PSC, the determination of efficient ETL/HTL materials other than the conventional ones, and the doping effect on charge extraction layers for increasing the efficiency of PSCs. Performing an EIS analysis helps to understand how these modifications alter the charge dynamics and recombination rate in the respective PSC. Here, we highlighted some of the recent studies that performed impedance spectroscopy to measure different perovskite solar cells. In Table 4, the effects of interfacial engineering, surface modification of perovskite layer, different cationic charges put on the charge transportation, and recombination in PSCs are summarized based on impedance spectroscopy analysis.

Table 4 A list of studies that determined the effects of interfacial engineering, surface modification of perovskite, and charge transport layer by performing impedance spectroscopy.

Perovskite device	Synthesis techniques	Bias voltage (V)	Frequency range (Hz)	Illumination	*Rs*	*Rt*	*Rrec*	Efficiency	Refs
RbBr w/o interfacial layer PSC	Dynamic three-step spin coating	1.05 V	1 MHz to 0.1 Hz	AM 1.5G (100 $mWcm^{-2}$)	-	67 Ω	-	16.33%	[167]
4 mg/mL RbBr interfacial layer PSC		1.1 V				50 Ω		18.39%	
Graded Pb/Sn PSC (Full-cell)		0 V	0.8 MHz to 1 Hz	illumination	21.9 Ω	218 Ω	6.37 kΩ	21.4%	[173]
Pb-based PSC (Full-cell)					35.9 Ω	329 Ω	3.47 kΩ	19.4%	
Mixed Pb/Sn PSC (Full-cell)					23.8 Ω	156 Ω	2.79 kΩ	10.5%	
W/o BIPH-II modified (control PSC)	Spin-coating	1 V	-	dark	58 Ω	-	1052 Ω	9.01%	[174]
With BIPH-II modified PSC					68 Ω		3112 Ω	17.31%	
PSC w/o MoO_3 interfacial layer	Spin-coating	1.04 V	1 MHz to 100 Hz	AM 1.5G (100 $mWcm^{-2}$)	-	22.6 Ω	175.5 Ω	11.2%	[175]
PSC with MoO_3 interfacial layer		1.10 V				26.6 Ω	220.6 Ω	13.5%	
c-PSC at 5 °C		0.8 V	1 MHz to 0.01 Hz			58.1 Ω	380.6 Ω	4.34%	[176]
c-PSC at 15 °C						59.4 Ω	374.1 Ω	8.34%	
c-PSC at 25 °C						54.3 Ω	343 Ω	12%	
c-PSC at 45 °C						59.4 Ω	335.3 Ω	5.5%	

PSC w/o AuNSs and SnO_2 (L1)	Spin-coating and Electron beam evaporation method (SnO_2)	-	1 MHz to 0.1 Hz	dark	-	-	219 Ω cm^2	18.07%	[177]
PSC with AuNSs and SnO_2 (L4)							329 Ω cm^2	20.31%	
PSC w/o FEA	Spin-coating	-0.8 V	1 MHz to 1 Hz	dark	-	4.02 kΩ	7.79 kΩ	16.74%	[178]
PSC with FEA-5 (5 mg/mL)						2.87 kΩ	9.49 kΩ	19.24%	
PSC with $PbTiO_3$ interfacial layer	Spin-coating	0.85 V	2 MHz to 0.1 Hz	dark	20.48 Ω		531.8 Ω	16.27%	[179]
PSC w/o $PbTiO_3$ interfacial layer					20.29 Ω		270.8 Ω	13.81%	
PSC-UV treated	functional molecular interface engineering (FMIE)	-	1 MHz to 1 kHz	dark	17.13 Ω	65.3 Ω	-	18.75%	[180]
PSC-PFN-Br treated					16.75 Ω	17.9 Ω		20.07%	
PSC-with P_3HT	Spin-coating	1 V	1 MHz to 1 Hz	dark	-	-	4884.6 Ω	6.49%	[181]
PSC w/o P_3HT							1770.4 Ω	5.09%	
PSC w/o CdS: $Cd(SCN_2H_4)_2Cl_2$	Spin-coating	0 V	1 MHz to 0.1 Hz	AM 1.5G	44.88 Ω cm^2	1202 mA cm^{-2}	1077 mA cm^{-2}	17.3%	[182]
PSC with CdS: $Cd(SCN_2H_4)_2Cl_2$					39.76 Ω cm^2	1345 mA cm^{-2}	1294 mA cm^{-2}	20.1%	
PSC with Cl additive	Spin-coating	0–1.11 V	2 MHz to 0.2 Hz	AM 1.5G	10.2 Ω (at 0 V)	-	-	19.43%	[183]
PSC w/o Cl additive		0–1.152 V			12.4 Ω (at 0 V)			21.2%	

PSC w/o chlorobenzene **PSC with chlorobenzene**	Spin coating	-	-	AM 1.5G	28 Ω 22 Ω	315 Ω 232 Ω	-	9.83% 12.91%	[184]
DMF-$(BA)_2(MA)_3Pb_4I_{13}$ PSC	Spin-coating with solvent based surface modification	-	-	-	21.7 Ω	723.5 Ω	-	9.81%	[185]
GBL-$(BA)_2(MA)_3Pb_4I_{13}$ PSC					18.3 Ω	631.6 Ω		11.7%	
3D-PSC **DJ-2D-3D-PSC**	Spin-coating	0.4	10^6 to 0.1 Hz	AM 1.5G	-	31 Ω 20 Ω	213 Ω 153 Ω	18.9% 21.6%	[186]

6. Photovoltaic Performance of PSCs

The first PSC was developed by Kojima et al. [11] in 2009 and showed a low efficiency of 3.8%. The maximum power conversion efficiency achieved was 25.7% for a certified perovskite-based solar cell [187]. To determine the power conversion efficiency of a solar cell and extract other parameters of the device, such as open circuit voltage (V_{OC}), short circuit current density (J_{SC}), fill factor (*FF*), etc., dark and illuminated *J-V* measurements of the cell are performed. The dark and illuminated response of a perovskite solar cell can provide valuable information. The dark *J-V* response of a solar cell is similar to that of a single junction diode model developed by Shockley. Based on the dark response, the shunt resistance (R_{sh}), series resistance (R_s), and diode quality factor of PSCs can be easily calculated. The performance of a PSC depends on several factors, such as perovskite film morphology, composition, device architecture, interface qualities, etc. In a poorly performing device, the V_{OC} is limited due to various losses that occur in the bulk perovskite and at the interface between the ETL or HTL and the perovskite layers. Various losses that occur at the interfaces were summarized by Stolterfoht et al., who investigated the effect of various charge transport layer interfaces on the perovskite absorber layer [188]. The typical *J-V* response and scan-dependent *J-V* response of perovskite solar cells are shown in Figures 10a and 10b, respectively.

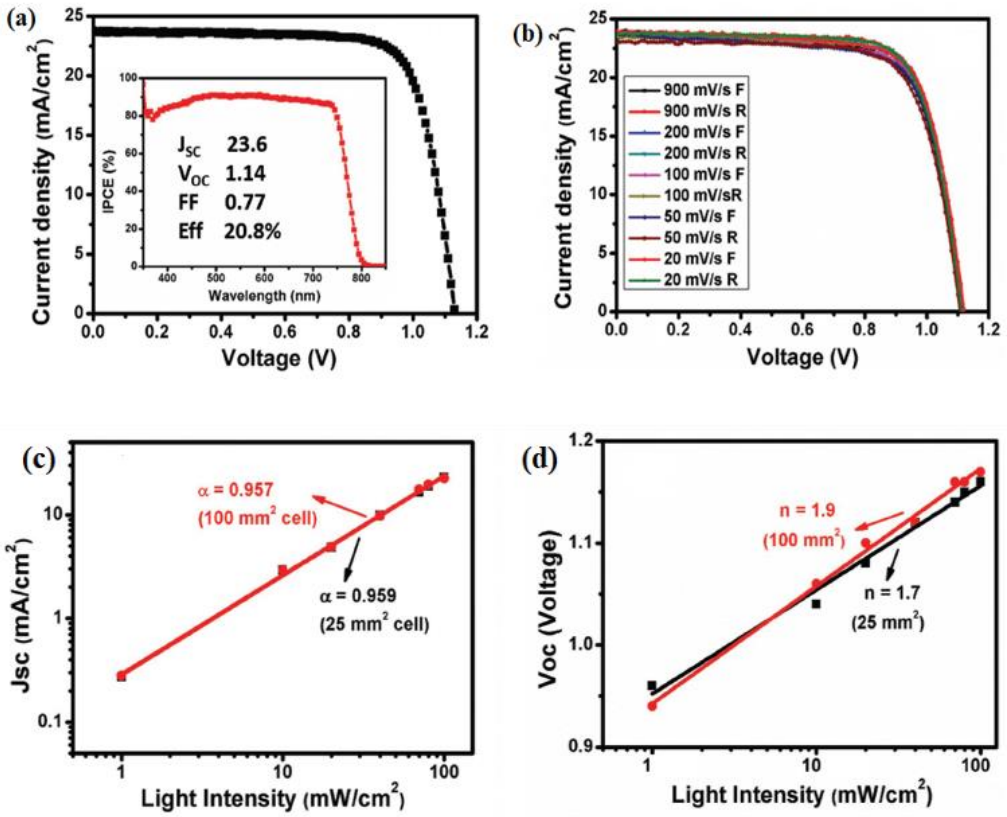

Figure 10 (a) The *J-V* response of PSCs. (b) Scan-dependent *J–V* curves. (c) Short circuit current, J_{SC} vs. light intensity. (d) Open circuit voltage, V_{OC} vs. light intensity [77].

Due to solution processability of perovskite thin films, PSCs are susceptible to bulk and interfacial defects. These defects result in non-radiative recombination, which leads to V_{OC} losses. The V_{OC} of a device decreases with log(ß) of the recombination process (non-radiative in the case of PSCs), where ß is the rate of the recombination process. The V_{OC} of a solar cell increases with log(I), where 'I'

indicates the intensity of incident light. The V_{OC} of the device decreases with an increase in the temperature because of the increase in the reverse saturation current of the diode. The plots for the light intensity dependence of J_{SC} and V_{OC} of PSCs are shown in Figures 9c and 9d, respectively. From the plot of light intensity vs. J_{SC}, the magnitude of recombination in perovskite can be determined, and from the plot of light intensity vs. *Voc*, diode ideality can be calculated. The J_{SC} value has an upper limit because of the presence of a bandgap in the semiconducting material; the bandgap regulates the onset of absorption of the photons present in solar flux. Thus, a material with a higher bandgap has a high V_{OC} but a low J_{SC} value because absorption starts at lower wavelengths or higher frequencies. The J_{SC} of a solar cell decreases due to the external quantum efficiency (EQE) of the solar cell. The EQE is the ratio of the number of electron-hole pairs extracted in an external load divided by the number of photons incident on the solar cell. Ideally, a solar cell can have 100% EQE if no loss occurs due to recombination or due to the collection of charge carriers; the J_{SC} value can be calculated in this case by simply integrating the EQE spectrum with photon flux at each wavelength. For materials with 100% EQE, the number of photons above the cut-off wavelength can be counted, and this can be converted into an equivalent J_{SC} value for the device. Practical solar cells have lower values of J_{SC} as achieving 100% EQE is impossible because of various factors, such as reflection at the front surface, recombination inside the absorber, parasitic absorption, and bad charge carrier collection at the contact and absorber interface. The J_{SC} value of a solar cell increases linearly with an increase in light intensity (I) and increases by a small amount by increasing the operating temperature of the device. The internal quantum efficiency (IQE) is the number of electron-hole pairs generated divided by the number of photons incident on the solar cell, if all the photons incident on the cell get absorbed (reflection and transmission losses are avoided). A low IQE indicates the absorber layer of the solar cell collects the photons incident on it inefficiently. The value of the IQE is always greater than that of the EQE and can be measured from the EQE of the solar cell. The value of R_{sh} can be calculated from the slope of log(*J*) and the voltage *V* when $V<<V_t$ (thermal voltage 25.9 eV at T = 300 K). Similarly, from the slope at a high current level for $V>>V_t$, the series resistance can be estimated. Shockley's single diode model contains information about the quasi-neutral region and the space charge region of the p-n junction solar cells. Generation or recombination of charge carriers in these regions can deviate the ideal *J-V* curve and modify the diode equation by a factor commonly known as the diode quality factor 'n'. The value of n can be determined from the slope of log(*J*) vs. *V*. The value of n for a diode varies between 1 and 2. When n = 1 (ideal case; Shockley model), the total current in the device is transported due to diffusion only, and the material of the system only has radiative recombination or bimolecular recombination. When n = 2, the device has many defects, and the current is limited due to Shockley-Read-Hall (SRH) recombination [189, 190]. Thus, determining the diode quality factor can indirectly inform about the defects present in the material. Determining the diode quality factor can help to assess the dominating recombination mechanism and find the balance between drift and diffusion current in solar cells. When drift current dominates, the solar current is limited due to space-charge-limited current [191]. This usually occurs at low injection levels. At a high injection limit, diffusion current dominates due to the built-in potential, and the current in solar cells increases exponentially with the voltage.

Some structures of perovskite solar cells might show peculiar but major problems, where the *J-V* response of the solar cells depends on the history of measurement. This phenomenon is commonly known as hysteresis. Hysteresis in *J-V* response occurs when the forward and backward

scans of voltage yield different *J-V* responses, which in turn yield different values for the PCE of the same device. The *J-V* hysteresis is a major unsolved problem hindering perovskite industrialization. Multiple explanations, such as the dependence on voltage scan speed, device architecture [192], ferroelectric polarization [193], ion migration [194], and capacitive charge storage, have been provided. McGehee et al. [195] reported the effect of different biases on the photovoltaic performance of PSCs. They found that the application of high positive bias led to an increase in fill factor and short circuit current, which improved the photovoltaic performance. Bisquert et al. [196] found that PSCs have a capacitive nature, which lowers the photo-voltage. Park et al. [197] investigated the effects of reverse and forward scans on photovoltaic performance and further added that under the forward bias condition, increasing the applied bias leads to a negative capacitive current, which results in a small value of the photocurrent. Thus, the hysteresis in the *J-V* curve can be suppressed by managing these parameters.

7. Stability Issues of PSCs

The efficiency of PSCs is close to the maximum theoretical value; however, stability is the major problem that needs to be addressed for its real-time applications. The stability of PSCs depends on extrinsic factors (temperature, moisture, oxygen, light, etc.) and intrinsic factors (ion migration, trap states, etc.) [198]. For example, when exposed to moisture, air, and temperatures above 55 °C, $MAPbI_3$-based PSCs show a structural phase shift and rapidly deteriorate above 85 °C [4]. In a moist environment, water molecules form hydrogen bonds with the organic part, thus weakening the bonds between the A-site organic cation and the PbX_6 octahedron. Additionally, water molecules protonate iodides resulting in the formation of HI, which further accelerates degradation. Atmospheric oxygen gets adsorbed on the vacant surfaces of perovskite and diffuses mainly through iodide vacancies, resulting in the formation of superoxide when it traps photogenerated electrons [199]. The highly active superoxide starts an acid-base reaction with acidic A-site cation resulting in the degradation of perovskite. Additionally, metallic contacts form metal halides when they react with iodine/iodide species. The reaction occurs as the iodine/iodide species diffuse to the metallic back-contact, or the metallic species diffuse to the perovskite layer. The effects of extrinsic conditions, such as humidity, temperature, UV light, and oxygen can be overcome by proper encapsulation of the PSC device. However, intrinsic factors, such as ion migration caused during *J-V* measurement under illumination and the applied external electric field, are unavoidable [150]. This leads to hysteresis in *the J-V* curve depending on the scan rate and direction. To evaluate the effect of the intrinsic factors under illumination and load on the solar cell stability test in an inert atmosphere, removing the effects of extrinsic factors is necessary to get more reliable data. Thus, ensuring the stability of PSCs under operating conditions is the most important step in their commercialization. Some studies conducted the stability test by leaving the devices in the dark or under inert conditions and periodically measuring them. However, such methods of testing stability do not correspond to real operational stability. Many protocols for device fabrication and measurement were followed by various groups, which made it challenging to reproduce and understand the degradation mechanism. Thus, adopting a standard protocol to characterize PSCs might help to make a fair comparison of the lifetime of the devices fabricated in different laboratories. The International Summit on Organic Photovoltaic Stability (ISOS) suggested that the stability test protocol should include tests performed under dark (ISOS-D), light (ISOS-L), outdoor

(ISOS-O), thermal cycling (ISOS-T), and light cycling (ISOS-LC) conditions [200]. The ISOS-D test includes ISOS-D-1, ISOS-D2, and ISOS-D-3, where the solar cells are stored in the dark and exposed to oxygen, moisture, and high temperature. It provides information on the shelf life of the perovskite material. In the ISOS-D-1 test, solar cells are tested at room temperature. Heat is responsible for thermally activated decomposition. Decomposition occurs on defective surfaces and interfaces since molecules possess higher energy at the defect site. Heat accelerates the diffusion/migration of ions. To study the effect at elevated temperatures under dark conditions, the ISOS-D-2 test is conducted at 65 °C and 85 °C. In the ISOS-D-3 test, relative humidity of 85% is considered along with a temperature of 65 °C and 85 °C. Light accelerates moisture-induced and O_2-induced decomposition. Continuous illumination causes ion migration and compositional degradation in perovskite. It also causes reversible phase segregation in the case of high Br substitution in mixed halide perovskite. To study the detrimental effect of light, the ISOS-L (light soaking) test is performed. In the outdoor stability test, denoted as ISOS-O, the solar cells are aged under sunlight and ambient conditions. In the ISOS-O-1 and ISOS-O-2 tests, *J-V* measurements are performed periodically under illumination by a solar simulator and under natural sunlight, respectively. In the ISOS-O-3 protocol, *J-V* measurements are performed by a solar simulator and in-situ maximum power point tracking (MPPT) under natural sunlight.

The maximum power point tracking (MPPT) for the thermal stability of perovskite solar cells is very important for the future commercialization of these devices. Tracking PCE retention with time in perovskite solar cells can help to determine the viability of these devices compared to other matured silicon solar cell technologies, such as Si and GaAs. Many researchers have studied the stability of perovskite solar cells using the maximum PCE tracking method. Saliba et al. studied the effect of device hysteresis on measuring the stabilized efficiency of perovskite solar cells and also discussed the aging test where maximum power point tracking was studied [201]. The aging data were extracted from the maximum power point current (J_{MPP}), voltage (V_{MPP}), and PCE. The researchers found that the value of J_{MPP} increased progressively compared to the same parameters extracted from the MPPT condition. The V_{MPP} did not show any clear trend but PCE followed the J_{MPP} trend. Such a trend was observed because the perovskite solar cell hysteresis became more pronounced with the aging of the cell. Ghosh et al. studied the long-term stability of perovskite solar cells that were fabricated under ambient conditions. The analysis was performed with devices that had an active area of 9 mm^2 without encapsulation under ambient conditions of 45–60% relative humidity [202]. The authors studied the effect of metal-back-contact on the performance of PSC and the long-term stability. They found that after recycling of the metal-back-contact the PSCs can be operated at maximum PCE for a longer duration. Rakocevic et al. proposed a two-step MPPT measuring procedure for comparing perovskite-based solar cells [203]. The authors first defined the optimal measurement delay based on the transient current density measurement, and then, determined the performance of the solar cell at the maximum power point. Köbler et al. studied the high-throughput aging system for parallel maximum power point tracking of perovskite solar cells capable of assessing many devices and discussed the system design [204].

The bandgap tunable property of perovskites allows the development of wide bandgap perovskites that are suitable for multi-junction solar cells. Besides their excellent optoelectronic properties, the solution processability features of perovskites make them interesting to fabricate tandem solar cells. Wide bandgap perovskites are promising as a top cell absorber in tandem solar cells. For developing high-efficiency tandem solar cells, the bandgap requirement for the top cell is

above 1.7 eV and the bottom cell bandgap should be in the range of 0.9–1.2 eV. Wide bandgap hybrid perovskites have been used as the top cell with Si as the bottom for developing high-efficiency tandem solar cells [205]. Additionally, perovskite-perovskite-based tandem solar cells have also been studied by various groups [206]. The bandgap of mixed halide perovskites can be tuned easily by varying the halide composition; for example, the bandgap can be increased by increasing the bromine content. However, perovskites with higher bromine concentrations are affected by light-induced phase segregation. When light falls on a wide bandgap material with a high bromine content, the photoexcited charge carriers separate the halide ions resulting in the uneven distribution of halide ions (bromine-rich and iodine-rich regions); thus, forming different bandgaps within the same material. The stability of low-bandgap perovskites is low as most of them are composed of Sn and Pb, which increases their vulnerability to humidity [207].

8. Summary and Future Perspective

Halide perovskite as a light absorber is an excellent candidate for next-generation photovoltaic technology. A thorough understanding of its physical, chemical, and optoelectronic properties might make this material better than other existing solar cell technologies. The primary concern of perovskite-based solar cells is their instability under different environmental and operating conditions. Additionally, perovskite solar cells fabricated to date with higher PCEs are of a small active area (typically less than 5 mm^2). Thus, the fabrication of stable perovskite films with a large active area is essential to realize for commercial applications. Since its discovery, the scientific community (both in academia and the industry) and researchers worldwide have been trying to bring the PSCs into commercial applications by improving its PCE and stability along with large-area device fabrication. The performance of perovskite solar cells depends on various factors, including morphology, roughness, and the full surface coverage of the fabricated film. Different synthesis methods are used for fabricating perovskite films, resulting in different film properties. Generally, films fabricated using solution process methods are associated with pinholes and cracks, which decrease the shunt resistance resulting in leakage current. To understand the unique properties of perovskite, various microscopic and spectroscopic characterization techniques are required. In this article, some of the well-known techniques used for characterizing PSCs were discussed. However, some of these techniques might damage the sample during characterization. In such cases, the sample needs to be reproduced using the same experimental conditions, which can be expensive and time-consuming. For example, in SEM and TEM, a high-energy electron beam may damage the sample. In AFM, the tip of the microscope in contact mode may scratch the surface of the sample. A certain technique might damage a particular material but not others. It depends on the materials being characterized and the aim of the study. The damage caused during the test can be minimized by applying proper measuring parameters to the instrument. For example, while performing SEM, samples are coated with a thin metal layer before they are placed in the instrument. SEM is a destructive technique for analyzing perovskite materials to be used as an absorber layer in PSCs. However, PL, UV-visible, Raman, FTIR, and Impedance spectroscopy techniques are non-destructive methods for characterizing PSCs. Additionally, FTIR microscopy and AFM-IR are potential and advanced non-destructive techniques. They have the additional advantages of simultaneously mapping the chemical composition of the perovskite film and performing IR spectral analysis at the desired location. However, reports on the application of these techniques for characterizing PSCs

are limited. Like SEM and TEM, these techniques provide morphological, topographical, and compositional information but in a non-destructive manner. Therefore, non-destructive approaches can be used to quickly study the performance of PSCs and their degradation mechanism using a small amount of the material.

In this review, we discussed various important characterization techniques used to investigate PSCs with suitable examples. Although these techniques have accelerated and advanced studies on PSCs, they still have some limitations associated with perovskite materials. Most of these characterization techniques use high-energy probes of e-beams, X-rays, and lasers, which can harm the perovskite film. Moreover, perovskite films cannot be measured accurately using these techniques because of degradation and phase transition caused by pressure, heat, and moisture. However, careful measurements under controlled conditions are extremely important and might help to solve some of the above-mentioned problems. For example, to prevent phase transition problems during measurements, cryotemperature techniques can be applied. To summarize, proper optimization of these techniques and further studies can provide a better understanding of the extraordinary characteristics and the degradation mechanism of this solar cell technology and also help to improve the efficiency and stability of the device. Advancements in these characterizing techniques will strongly influence the progress of research on PSCs.

Acknowledgments

T.S acknowledges support from the Science and Engineering Research Board (SERB) with Grant no SRG/2019/1303 and Sponsored Research and Industrial Consultancy (SRIC) IIT Kharagpur for providing infrastructure facilities. B.B, S.P, D.K, S.M, S. G and S. K. acknowledge to IIT Kharagpur for research fellowship.

Author Contributions

B.B conceptualized the work and prepared the manuscript. S.P helped in writing the manuscript and editing D.K helped in writing the manuscript and editing S.M helped in writing the manuscript and editing, S. G helped in writing the manuscript and proof reading and S. K helped in writing the manuscript and editing, A.C reviewed the work and corrected the manuscript, T.S supervised (conceive the idea, writing, editing) the complete work.

Funding

T.S acknowledges support from the Science and Engineering Research Board (SERB) with Grant no SRG/2019/1303 and Sponsored Research and Industrial Consultancy (SRIC) IIT Kharagpur for providing infrastructure facilities.

Competing Interests

The authors have declared that no competing interests exist.

References

1. Schouwink P, Ley MB, Tissot A, Hagemann H, Jensen TR, Smrčok L, et al. Structure and

properties of complex hydride perovskite materials. Nat Commun. 2014; 5: 5706.
2. Jeon NJ, Noh JH, Yang WS, Kim YC, Ryu S, Seo J, et al. Compositional engineering of perovskite materials for high-performance solar cells. Nature. 2015; 517: 476-480.
3. Grätzel M. The light and shade of perovskite solar cells. Nat Mater. 2014; 13: 838-842.
4. Jena AK, Kulkarni A, Miyasaka T. Halide perovskite photovoltaics: Background, status, and future prospects. Chem Rev. 2019; 119: 3036-3103.
5. Snaith HJ. Perovskites: The emergence of a new era for low-cost, high-efficiency solar cells. J Phys Chem Lett. 2013; 4: 3623-3630.
6. Stranks SD, Eperon GE, Grancini G, Menelaou C, Alcocer MJ, Leijtens T, et al. Electron-hole diffusion lengths exceeding 1 micrometer in an organometal trihalide perovskite absorber. Science. 2013; 342: 341-344.
7. Mishra S, Ghosh S, Singh T. Progress in materials development for flexible perovskite solar cells and future prospects. ChemSusChem. 2021; 14: 512-538.
8. Wojciechowski K, Stranks SD, Abate A, Sadoughi G, Sadhanala A, Kopidakis N, et al. Heterojunction modification for highly efficient organic-inorganic perovskite solar cells. ACS Nano. 2014; 8: 12701-12709.
9. Singh T, Singh J, Miyasaka T. Role of metal oxide electron-transport layer modification on the stability of high performing perovskite solar cells. ChemSusChem. 2016; 9: 2559-2566.
10. Yousaf SA, Imran M, Ikram M, Ali S. The critical role of metal oxide electron transport layer for perovskite solar cell. Appl Nanosci. 2018; 8: 1515-1522.
11. Minemoto T, Kawano Y, Nishimura T, Shen Q, Kenji Y, Iikubo S, et al. Theoretical analysis of band alignment at back junction in Sn-Ge perovskite solar cells with inverted p-i-n structure. Sol Energy Mater Sol Cells. 2020; 206: 110268.
12. Kojima A, Teshima K, Shirai Y, Miyasaka T. Organometal halide perovskites as visible-light sensitizers for photovoltaic cells. J Am Chem Soc. 2009; 131: 6050-6051.
13. Im JH, Lee CR, Lee JW, Park SW, Park NG. 6.5% efficient perovskite quantum-dot-sensitized solar cell. Nanoscale. 2011; 3: 4088-4093.
14. Lee MM, Teuscher J, Miyasaka T, Murakami TN, Snaith HJ. Efficient hybrid solar cells based on meso-superstructured organometal halide perovskites. Science. 2012; 338: 643-647.
15. Kim HS, Lee CR, Im JH, Lee KB, Moehl T, Marchioro A, et al. Lead iodide perovskite sensitized all-solid-state submicron thin film mesoscopic solar cell with efficiency exceeding 9%. Sci Rep. 2012; 2: 591.
16. Etgar L, Gao P, Xue Z, Peng Q, Chandiran AK, Liu B, et al. Mesoscopic $CH_3NH_3PbI_3/TiO_2$ heterojunction solar cells. J Am Chem Soc. 2012; 134: 17396-17399.
17. Best research-cell efficiency chart [Internet]. Golden: NREL; [cited date 2022 March 2]. Aviailable from: https://www.nrel.gov/pv/cell-efficiency.html.
18. Lu YB, Cong WY, Guan C, Sun H, Xin Y, Wang K, et al. Light enhanced moisture degradation of perovskite solar cell material $CH_3NH_3PbI_3$. J Mater Chem A. 2019; 7: 27469-27474.
19. Kundu S, Kelly TL. In situ studies of the degradation mechanisms of perovskite solar cells. EcoMat. 2020; 2: e12025.
20. Idígoras J, Aparicio FJ, Contreras-Bernal L, Ramos-Terrón S, Alcaire M, Sánchez-Valencia JR, et al. Enhancing moisture and water resistance in perovskite solar cells by encapsulation with ultrathin plasma polymers. ACS Appl Mater Interfaces. 2018; 10: 11587-11594.
21. Manshor NA, Wali Q, Wong KK, Muzakir SK, Fakharuddin A, Schmidt-Mende L, et al. Humidity

versus photo-stability of metal halide perovskite films in a polymer matrix. Phys Chem Chem Phys. 2016; 18: 21629-21639.
22. Kopacic I, Friesenbichler B, Hoefler SF, Kunert B, Plank H, Rath T, et al. Enhanced performance of germanium halide perovskite solar cells through compositional engineering. ACS Appl Energy Mater. 2018; 1: 343-347.
23. Chen M, Ju MG, Garces HF, Carl AD, Ono LK, Hawash Z, et al. Highly stable and efficient all-inorganic lead-free perovskite solar cells with native-oxide passivation. Nat Commun. 2019; 10: 16.
24. Jain SM, Edvinsson T, Durrant JR. Green fabrication of stable lead-free bismuth based perovskite solar cells using a non-toxic solvent. Commun Chem. 2019; 2: 91.
25. Baranwal AK, Masutani H, Sugita H, Kanda H, Kanaya S, Shibayama N, et al. Lead-free perovskite solar cells using Sb and Bi-based $A_3B_2X_9$ and A_3BX_6 crystals with normal and inverse cell structures. Nano Converg. 2017; 4: 26.
26. Singh T, Öz S, Sasinska A, Frohnhoven R, Mathur S, Miyasaka T. Sulfate-assisted interfacial engineering for high yield and efficiency of triple cation perovskite solar cells with alkali-doped TiO_2 electron-transporting layers. Adv Funct Mater. 2018; 28: 1706287.
27. Ikram M, Malik R, Raees R, Imran M, Wang F, Ali S, et al. Recent advancements and future insight of lead-free non-toxic perovskite solar cells for sustainable and clean energy production: A review. Sustain Energy Technol Assessments. 2022; 53: 102433.
28. Liao M, Yu BB, Jin Z, Chen W, Zhu Y, Zhang X, et al. Efficient and stable FASnI3 perovskite solar cells with effective interface modulation by low-dimensional perovskite layer. ChemSusChem. 2019; 12: 5007-5014.
29. Singh T, Kulkarni A, Ikegami M, Miyasaka T. Effect of electron transporting layer on bismuth-based lead-free perovskite $(CH_3NH_3)_3$ Bi_2I_9 for photovoltaic applications. ACS Appl Mater Interfaces. 2016; 8: 14542-14547.
30. Schlipf J, Hu Y, Pratap S, Bießmann L, Hohn N, Porcar L, et al. Shedding light on the moisture stability of 3D/2D hybrid perovskite heterojunction thin films. ACS Appl Energy Mater. 2019; 2: 1011-1018.
31. Alidaei M, Ahmadi V, Mousavi SM, Roghabadi FA. Stability improvement of perovskite solar cell using photoswitchable and moisture resistant dual-function interfacial layer. J Alloys Compd. 2022; 903: 163891.
32. Ali Ahmad SO, Ashfaq A, Akbar MU, Ikram M, Khan K, Wang F, et al. Application of two-dimensional materials in perovskite solar cells: Recent progress, challenges, and prospective solutions. J Mater Chem C. 2021; 9: 14065-14092.
33. Tumen-Ulzii G, Matsushima T, Klotz D, Leyden MR, Wang P, Qin C, et al. Hysteresis-less and stable perovskite solar cells with a self-assembled monolayer. Commun Mater. 2020; 1: 31.
34. Manser JS, Saidaminov MI, Christians JA, Bakr OM, Kamat PV. Making and breaking of lead halide perovskites. Acc Chem Res. 2016; 49: 330-338.
35. Hanusch FC, Wiesenmayer E, Mankel E, Binek A, Angloher P, Fraunhofer C, et al. Efficient planar heterojunction perovskite solar cells based on formamidinium lead bromide. J Phys Chem Lett. 2014; 5: 2791-2795.
36. Unger EL, Bowring AR, Tassone CJ, Pool VL, Gold-Parker A, Cheacharoen R, et al. Chloride in lead chloride-derived organo-metal halides for perovskite-absorber solar cells. Chem Mater. 2014; 26: 7158-7165.

37. Pool VL, Dou B, Van Campen DG, Klein-Stockert TR, Barnes FS, Shaheen SE, et al. Thermal engineering of $FAPbI_3$ perovskite material via radiative thermal annealing and in situ XRD. Nat Commun. 2017; 8: 14075.
38. Ma D, Mora-Seró I, Saliba M, Etgar L. Energy spotlight. ACS Energy Lett. 2021; 6: 3750-3752.
39. Yadavalli SK, Zhou Y, Padture NP. Exceptional grain growth in formamidinium lead iodide perovskite thin films induced by the δ-to-α phase transformation. ACS Energy Lett. 2018; 3: 63-64.
40. Tan KW, Moore DT, Saliba M, Sai H, Estroff LA, Hanrath T, et al. Thermally induced structural evolution and performance of mesoporous block copolymer-directed alumina perovskite solar cells. ACS Nano. 2014; 8: 4730-4739.
41. Barrows AT, Lilliu S, Pearson AJ, Babonneau D, Dunbar ADF, Lidzey DG. Monitoring the formation of a $CH_3NH_3PbI_{3-x}CL_x$ perovskite during thermal annealing using X-ray scattering. Adv Funct Mater. 2016; 26: 4934-4942.
42. Moore DT, Sai H, Tan KW, Smilgies DM, Zhang W, Snaith HJ, et al. Crystallization kinetics of organic-inorganic trihalide perovskites and the role of the lead anion in crystal growth. J Am Chem Soc. 2015; 137: 2350-2358.
43. Saliba M, Tan KW, Sai H, Moore DT, Scott T, Zhang W, et al. Influence of thermal processing protocol upon the crystallization and photovoltaic performance of organic–inorganic lead trihalide perovskites. J Phys Chem C. 2014; 118: 17171-17177.
44. Huang L, Hu Z, Xu J, Zhang K, Zhang J, Zhu Y. Multi-step slow annealing perovskite films for high performance planar perovskite solar cells. Sol Energy Mater Sol Cells. 2015; 141: 377-382.
45. Xiao X, Dai J, Fang Y, Zhao J, Zheng X, Tang S, et al. Suppressed ion migration along the in-plane direction in layered perovskites. ACS Energy Lett. 2018; 3: 684-688.
46. Tailor NK, Satapathi S. The impact of $Cs_3Bi_2Cl_9$ single crystal growth modality on its symmetry and morphology. J Mater Res Technol. 2020; 9: 7149-7157.
47. Chen Z, Dong Q, Liu Y, Bao C, Fang Y, Lin Y, et al. Thin single crystal perovskite solar cells to harvest below-bandgap light absorption. Nat Commun. 2017; 8: 1890.
48. Liu F, Sommer F, Bos C, Mittemeijer EJ. Analysis of solid state phase transformation kinetics: Models and recipes. Int Mater Rev. 2007; 52: 193-212.
49. Ren Y, Oswald IWH, Wang X, McCandless GT, Chan JY. Orientation of organic cations in hybrid inorganic–organic perovskite $CH_3NH_3PbI_3$ from subatomic resolution single crystal neutron diffraction structural studies. Cryst Growth Des. 2016; 16: 2945-2951.
50. Weller MT, Weber OJ, Henry PF, Di Pumpo AM, Hansen TC. Complete structure and cation orientation in the perovskite photovoltaic methylammonium lead iodide between 100 and 352 k. Chem Commun. 2015; 51: 4180-4183.
51. Mashiyama H, Kurihara Y, Azetsu T. Disordered cubic perovskite structure of $CH_3NH_3PbX_3$ (X = Cl, Br, I). J Korean Phys Soc. 1998; 32: S156-S158.
52. Stoumpos CC, Malliakas CD, Kanatzidis MG. Semiconducting tin and lead iodide perovskites with organic cations: Phase transitions, high mobilities, and near-infrared photoluminescent properties. Inorg Chem. 2013; 52: 9019-9038.
53. Kawamura Y, Mashiyama H, Hasebe K. Structural study on cubic-tetragonal transition of $CH_3NH_3PbI_3$. J Phys Soc Japan. 2002; 71: 1694-1697.
54. Baikie T, Fang Y, Kadro JM, Schreyer M, Wei F, Mhaisalkar SG, et al. Synthesis and crystal chemistry of the hybrid perovskite $(CH_3NH_3)PbI_3$ for solid-state sensitised solar cell applications.

J Mater Chem A. 2013; 1: 5628-5641.
55. Chen T, Foley BJ, Ipek B, Tyagi M, Copley JR, Brown CM, et al. Rotational dynamics of organic cations in the $CH_3NH_3PbI_3$ perovskite. Phys Chem Chem Phys. 2015; 17: 31278-31286.
56. Mashiyama H, Kawamura Y, Magome E, Kubota Y. Displacive character of the cubic-tetragonal transition in $CH_3NH_3PbI_3$. J Korean Phys Soc. 2003; 42: S1026-S1029.
57. Poglitsch A, Weber D. Dynamic disorder in methylammoniumtrihalogenoplumbates (II) observed by millimeter-wave spectroscopy. J Chem Phys. 1987; 87: 6373-6378.
58. Sutton RJ, Filip MR, Haghighirad AA, Sakai N, Wenger B, Giustino F, et al. Cubic or orthorhombic? Revealing the crystal structure of metastable black-phase $CsPbI_3$ by theory and experiment. ACS Energy Lett. 2018; 3: 1787-1794.
59. Chung I, Song JH, Im J, Androulakis J, Malliakas CD, Li H, et al. $CsSnI_3$: Semiconductor or metal? High electrical conductivity and strong near-infrared photoluminescence from a single material. High hole mobility and phase-transitions. J Am Chem Soc. 2012; 134: 8579-8587.
60. Scaife DE, Weller PF, Fisher WG. Crystal preparation and properties of cesium tin(II) trihalides. J Solid State Chem. 1974; 9: 308-314.
61. Oku T. Crystal structures of $CH_3NH_3PbI_3$ and related perovskite compounds used for solar cells. In: Solar cells: New approaches and reviews. Rijeka: IntechOpen; 2015. pp. 77-102.
62. Thiele G, Rotter HW, Schmidt KD. Kristallstrukturen und phasentransformationen von caesiumtrihalogenogermanaten(II) $CsGeX_3$ (x = Cl, Br, I). Z Anorg Allg Chem. 1987; 545: 148-156.
63. Wei F, Deng Z, Sun S, Zhang F, Evans DM, Kieslich G, et al. Synthesis and properties of a lead-free hybrid double perovskite: $(CH_3NH_3)_2AgBiBr_6$. Chem Mater. 2017; 29: 1089-1094.
64. Wei F, Deng Z, Sun S, Xie F, Kieslich G, Evans DM, et al. The synthesis, structure and electronic properties of a lead-free hybrid inorganic–organic double perovskite $(MA)_2KBiCl_6$ (MA = methylammonium). Mater Horizons. 2016; 3: 328-332.
65. Majher JD, Gray MB, Strom TA, Woodward PM. $Cs_2NaBiCl_6:Mn^{2+}$—A New orange-red halide double perovskite phosphor. Chem Mater. 2019; 31: 1738-1744.
66. Bohnsack A, Meyer G. Crystal structure of dirubidium lithium dysprosium (III) hexabromide, $Rb_2LiDyBr_6$. Z Krist-New Cryst St. 1997; 212: 2.
67. Stoumpos CC, Cao DH, Clark DJ, Young J, Rondinelli JM, Jang JI, et al. Ruddlesden–popper hybrid lead iodide perovskite 2D homologous semiconductors. Chem Mater. 2016; 28: 2852-2867.
68. Zhu XH, Mercier N, Allain M, Frère P, Blanchard P, Roncali J, et al. Crystal structure of (NH_3–*R*–NH_3)(NH_3–*R*–NH_2)PbI_5 (*R*=5,5′-bis(ethylsulfanyl)-2,2′-bithiophene): $NH_3^+\cdots NH$ interaction as a tool to reach densely packed organic layers in organic-inorganic perovskites. J Solid State Chem. 2004; 177: 1067-1071.
69. Yamada K, Sera H, Sawada S, Tada H, Okuda T, Tanaka H. Reconstructive phase transformation and kinetics of $Cs_3Sb_2I_9$ by means of rietveld analysis of X-ray diffraction and ^{127}I NQR. J Solid State Chem. 1997; 134: 319-325.
70. Zhao Y, Nardes AM, Zhu K. Solid-state mesostructured perovskite $CH_3NH_3PbI_3$ solar cells: Charge transport, recombination, and diffusion length. J Phys Chem Lett. 2014; 5: 490-494.
71. Ng A, Ren Z, Shen Q, Cheung SH, Gokkaya HC, So SK, et al. Crystal engineering for low defect density and high efficiency hybrid chemical vapor deposition grown perovskite solar cells. ACS Appl Mater Interfaces. 2016; 8: 32805-32814.
72. Lin G, Lin Y, Huang H, Cui R, Guo X, Liu B, et al. Novel exciton dissociation behavior in tin-lead organohalide perovskites. Nano Energy. 2016; 27: 638-646.

73. Burschka J, Pellet N, Moon SJ, Humphry-Baker R, Gao P, Nazeeruddin MK, et al. Sequential deposition as a route to high-performance perovskite-sensitized solar cells. Nature. 2013; 499: 316-319.
74. Kim HS, Hagfeldt A, Park NG. Morphological and compositional progress in halide perovskite solar cells. Chem Commun. 2019; 55: 1192-1200.
75. Ghosh S, Mishra S, Singh T. Antisolvents in perovskite solar cells: Importance, issues, and alternatives. Adv Mater Interfaces. 2020; 7: 2000950.
76. Ghosh S, Singh T. Role of ionic liquids in organic-inorganic metal halide perovskite solar cells efficiency and stability. Nano Energy. 2019; 63: 103828.
77. Singh T, Miyasaka T. Stabilizing the efficiency beyond 20% with a mixed cation perovskite solar cell fabricated in ambient air under controlled humidity. Adv Energy Mater. 2018; 8: 1700677.
78. Alkhalayfeh MA, Aziz AA, Pakhuruddin MZ, Katubi KMM. Recent advances of perovskite solar cells embedded with plasmonic nanoparticles. Phys Status Solidi A. 2021; 218: 2100310.
79. Ali A, Kang JH, Seo JH, Walker B. Effect of plasmonic ag nanoparticles on the performance of inverted perovskite solar cells. Adv Eng Mater. 2020; 22: 1900976.
80. Aamir M, Adhikari T, Sher M, Revaprasadu N, Khalid W, Akhtar J, et al. Fabrication of planar heterojunction $CsPbBr_2I$ perovskite solar cells using ZnO as an electron transport layer and improved solar energy conversion efficiency. New J Chem. 2018; 42: 14104-14110.
81. Yun AJ, Kim J, Hwang T, Park B. Origins of efficient perovskite solar cells with low-temperature processed SnO_2 electron transport layer. ACS Appl Energy Mater. 2019; 2: 3554-3560.
82. Liao W, Zhao D, Yu Y, Shrestha N, Ghimire K, Grice CR, et al. Fabrication of efficient low-bandgap perovskite solar cells by combining formamidinium tin iodide with methylammonium lead iodide. J Am Chem Soc. 2016; 138: 12360-12363.
83. Kamkar DA, Wang M, Wudl F, Nguyen TQ. Single nanowire opv properties of a fullerene-capped P3HT dyad investigated using conductive and photoconductive AFM. ACS Nano. 2012; 6: 1149-1157.
84. Yun JS, Ho-Baillie A, Huang S, Woo SH, Heo Y, Seidel J, et al. Benefit of grain boundaries in organic–inorganic halide planar perovskite solar cells. J Phys Chem Lett. 2015; 6: 875-880.
85. Kim T, Chu YH, Lee J, Cho SH, Kim S, Bang K, et al. Confined growth of high-quality single-crystal mapbbr3 by inverse temperature crystallization for photovoltaic applications. Electron Mater Lett. 2021; 17: 347-354.
86. Shao Y, Fang Y, Li T, Wang Q, Dong Q, Deng Y, et al. Grain boundary dominated ion migration in polycrystalline organic-inorganic halide perovskite films. Energy Environ Sci. 2016; 9: 1752-1759.
87. Li JJ, Ma JY, Hu JS, Wang D, Wan LJ. Influence of N,N-dimethylformamide annealing on the local electrical properties of organometal halide perovskite solar cells: An atomic force microscopy investigation. ACS Appl Mater Interfaces. 2016; 8: 26002-26007.
88. Thu Nguyen TT, Kim Y, Bae S, Bari M, Jung HR, Jo W, et al. Raman scattering studies of the structural phase transitions in single-crystalline $CH_3NH_3PbI_3$. J Phys Chem Lett. 2020; 11: 3773-3781.
89. Quarti C, Grancini G, Mosconi E, Bruno P, Ball JM, Lee MM, et al. The raman spectrum of the $CH_3NH_3PbI_3$ hybrid perovskite: Interplay of theory and experiment. J Phys Chem Lett. 2014; 5: 279-284.
90. Ruan S, McMeekin DP, Fan R, Webster NAS, Ebendorff-Heidepriem H, Cheng YB, et al. Raman spectroscopy of formamidinium-based lead halide perovskite single crystals. J Phys Chem C.

2020; 124: 2265-2272.
91. Kim BG, Jang W, Choa YH, Wang DH. Selective UV absorbance of copper chalcogenide nanoparticles for enhanced illumination durability in perovskite photovoltaics. ACS Sustain Chem Eng. 2020; 8: 7617-7627.
92. Ledinský M, Löper P, Niesen B, Holovský J, Moon SJ, Yum JH, et al. Raman spectroscopy of organic-inorganic halide perovskites. J Phys Chem Lett. 2015; 6: 401-406.
93. Pistor P, Ruiz A, Cabot A, Izquierdo-Roca V. Advanced raman spectroscopy of methylammonium lead iodide: Development of a non-destructive characterisation methodology. Sci Rep. 2016; 6: 35973.
94. Deepa M, Salado M, Calio L, Kazim S, Shivaprasad S, Ahmad S. Cesium power: Low Cs^+ levels impart stability to perovskite solar cells. Phys Chem Chem Phys. 2017; 19: 4069-4077.
95. Wu Z, Jiang M, Liu Z, Jamshaid A, Ono LK, Qi Y. Highly efficient perovskite solar cells enabled by multiple ligand passivation. Adv Energy Mater. 2020; 10: 1903696.
96. Zhang H, Shi J, Xu X, Zhu L, Luo Y, Li D, et al. Mg-doped TiO_2 boosts the efficiency of planar perovskite solar cells to exceed 19%. J Mater Chem A. 2016; 4: 15383-15389.
97. Das C, Wussler M, Hellmann T, Mayer T, Jaegermann W. In situ XPS study of the surface chemistry of MAPI solar cells under operating conditions in vacuum. Phys Chem Chem Phys. 2018; 20: 17180-17187.
98. Dong Q, Fang Y, Shao Y, Mulligan P, Qiu J, Cao L, et al. Electron-hole diffusion lengths > 175 μm in solution-grown $CH_3NH_3PbI_3$ single crystals. Science. 2015; 347: 967-970.
99. Xing J, Wang Q, Dong Q, Yuan Y, Fang Y, Huang J. Ultrafast ion migration in hybrid perovskite polycrystalline thin films under light and suppression in single crystals. Phys Chem Chem Phys. 2016; 18: 30484-30490.
100. Song Y, Bi W, Wang A, Liu X, Kang Y, Dong Q. Efficient lateral-structure perovskite single crystal solar cells with high operational stability. Nat Commun. 2020; 11: 274.
101. Divitini G, Cacovich S, Matteocci F, Cinà L, Di Carlo A, Ducati C. In situ observation of heat-induced degradation of perovskite solar cells. Nat Energy. 2016; 1: 15012.
102. Yang B, Dyck O, Ming W, Du MH, Das S, Rouleau CM, et al. Observation of nanoscale morphological and structural degradation in perovskite solar cells by in situ TEM. ACS Appl Mater Interfaces. 2016; 8: 32333-32340.
103. Kim TW, Shibayama N, Cojocaru L, Uchida S, Kondo T, Segawa H. Real-time in situ observation of microstructural change in organometal halide perovskite induced by thermal degradation. Adv Funct Mater. 2018; 28: 1804039.
104. Seo YH, Kim JH, Kim DH, Chung HS, Na SI. In situ TEM observation of the heat–induced degradation of single– and triple–cation planar perovskite solar cells. Nano Energy. 2020; 77: 105164.
105. Abdelmageed G, Jewell L, Hellier K, Seymour L, Luo B, Bridges F, et al. Mechanisms for light induced degradation in $MAPbI_3$ perovskite thin films and solar cells. Appl Phys Lett. 2016; 109: 233905.
106. Yu X, Qin Y, Peng Q. Probe decomposition of methylammonium lead iodide perovskite in N_2 and O_2 by in situ infrared spectroscopy. J Phys Chem A. 2017; 121: 1169-1174.
107. Gan Z, Yu Z, Meng M, Xia W, Zhang X. Hydration of mixed halide perovskites investigated by fourier transform infrared spectroscopy. APL Mater. 2019; 7: 031107.
108. Venkatesan S, Hao F, Kim J, Rong Y, Zhu Z, Liang Y, et al. Moisture-driven phase transition for

improved perovskite solar cells with reduced trap-state density. Nano Res. 2017; 10: 1413-1422.
109. Dhamaniya BP, Chhillar P, Roose B, Dutta V, Pathak SK. Unraveling the effect of crystal structure on degradation of methylammonium lead halide perovskite. ACS Appl Mater Interfaces. 2019; 11: 22228-22239.
110. Futscher MH, Lee JM, McGovern L, Muscarella LA, Wang T, Haider MI, et al. Quantification of ion migration in $CH_3NH_3PbI_3$ perovskite solar cells by transient capacitance measurements. Mater Horizons. 2019; 6: 1497-1503.
111. Lee JW, Kim SG, Yang JM, Yang Y, Park NG. Verification and mitigation of ion migration in perovskite solar cells. APL Mater. 2019; 7: 041111.
112. Zhou Y, Yin Y, Zuo X, Wang L, Li TD, Zhou Y, et al. Enhancing chemical stability and suppressing ion migration in $CH_3NH_3PbI_3$ perovskite solar cells via direct backbone attachment of polyesters on grain boundaries. Chem Mater. 2020; 32: 5104-5117.
113. Zheng L, Wang K, Zhu T, Yang Y, Chen R, Gu K, et al. High-performance perovskite solar cells by one-step self-assembled perovskite-polymer thin films. ACS Appl Energy Mater. 2020; 3: 5902-5912.
114. Papadatos D, Sygkridou D, Stathatos E. Carbon-based, novel triple cation mesoscopic perovskite solar cell fabricated entirely under ambient air conditions. Mater Lett. 2020; 268: 127621.
115. Afroz MA, Garai R, Gupta RK, Iyer PK. Additive-assisted defect passivation for minimization of open-circuit voltage loss and improved perovskite solar cell performance. ACS Appl Energy Mater. 2021; 4: 10468-10476.
116. Xiong J, Samanta PN, Qi Y, Demeritte T, Williams K, Leszczynski J, et al. Enhanced perovskite solar cell performance via 2-amino-5-iodobenzoic acid passivation. ACS Appl Mater Interfaces. 2022; 14: 5414-5424.
117. Gupta RK, Garai R, Iyer PK. Ambient stable perovskite solar cells through trifluoro acetic acid-mediated multifunctional anchoring. ACS Appl Energy Mater. 2022; 5: 1571-1579.
118. Yang Y, Liang J, Zhang Z, Tian C, Wu X, Zheng Y, et al. Suppressing residual lead iodide and defects in sequential-deposited perovskite solar cell via bidentate potassium dichloroacetate ligand. ChemSusChem. 2022; 15: e202102474.
119. Garai R, Gupta RK, Tanwar AS, Hossain M, Iyer PK. Conjugated polyelectrolyte-passivated stable perovskite solar cells for efficiency beyond 20%. Chem Mater. 2021; 33: 5709-5717.
120. Kim JH, Kim SG, Park NG. Effect of chemical bonding nature of post-treatment materials on photovoltaic performance of perovskite solar cells. ACS Energy Lett. 2021; 6: 3435-3442.
121. Han TH, Lee JW, Choi C, Tan S, Lee C, Zhao Y, et al. Perovskite-polymer composite cross-linker approach for highly-stable and efficient perovskite solar cells. Nat Commun. 2019; 10: 520.
122. Troughton J, Hooper K, Watson TM. Humidity resistant fabrication of $CH_3NH_3PbI_3$ perovskite solar cells and modules. Nano Energy. 2017; 39: 60-68.
123. Guo X, McCleese C, Kolodziej C, Samia AC, Zhao Y, Burda C. Identification and characterization of the intermediate phase in hybrid organic–inorganic $MAPbI_3$ perovskite. Dalt Trans. 2016; 45: 3806-3813.
124. Jeon NJ, Noh JH, Kim YC, Yang WS, Ryu S, Seok SI. Solvent engineering for high-performance inorganic–organic hybrid perovskite solar cells. Nat Mater. 2014; 13: 897-903.
125. Zhang W, Jiang Y, Ding Y, Zheng M, Wu S, Lu X, et al. Solvent-induced textured structure and improved crystallinity for high performance perovskite solar cells. Opt Mater Express. 2017; 7: 2150-2160.

126. Ahn N, Son DY, Jang IH, Kang SM, Choi M, Park NG. Highly reproducible perovskite solar cells with average efficiency of 18.3% and best efficiency of 19.7% fabricated via lewis base adduct of lead(II) iodide. J Am Chem Soc. 2015; 137: 8696-8699.
127. Zuo L, Dong S, De Marco N, Hsieh YT, Bae SH, Sun P, et al. Morphology evolution of high efficiency perovskite solar cells via vapor induced intermediate phases. J Am Chem Soc. 2016; 138: 15710-15716.
128. Tirado J, Vásquez-Montoya M, Roldán-Carmona C, Ralaiarisoa M, Koch N, Nazeeruddin MK, et al. Air-stable n–i–p planar perovskite solar cells using nickel oxide nanocrystals as sole hole-transporting material. ACS Appl Energy Mater. 2019; 2: 4890-4899.
129. Shit A, Nandi AK. Interface engineering of hybrid perovskite solar cells with poly(3-thiophene acetic acid) under ambient conditions. Phys Chem Chem Phys. 2016; 18: 10182-10190.
130. Glaser T, Müller C, Sendner M, Krekeler C, Semonin OE, Hull TD, et al. Infrared spectroscopic study of vibrational modes in methylammonium lead halide perovskites. J Phys Chem Lett. 2015; 6: 2913-2918.
131. Sarkar P, Srivastava A, Tripathy SK, Baishnab KL, Lenka TR, Menon PS, et al. Impact of Sn doping on methylammonium lead chloride perovskite: An experimental study. J Appl Phys. 2020; 127: 125110.
132. Cherrette VL, Hutcherson CJ, Barnett JL, So MC. Fabrication and characterization of perovskite solar cells: An integrated laboratory experience. J Chem Educ. 2018; 95: 631-635.
133. Almeida MAP, Maciel AP. Optical spectroscopy and its applications in inorganic materials. In: Handbook of materials characterization. Cham: Springer; 2018. pp. 293-315.
134. Kulkarni SA, Baikie T, Boix PP, Yantara N, Mathews N, Mhaisalkar S. Band-gap tuning of lead halide perovskites using a sequential deposition process. J Mater Chem A. 2014; 2: 9221-9225.
135. Hu H, Ren Z, Fong PWK, Qin M, Liu D, Lei D, et al. Room-temperature meniscus coating of >20% perovskite solar cells: A film formation mechanism investigation. Adv Funct Mater. 2019; 29: 1900092.
136. Bhaumik S, Ray S, Batabyal SK. Recent advances of lead-free metal halide perovskite single crystals and nanocrystals: Synthesis, crystal structure, optical properties, and their diverse applications. Mater Today Chem. 2020; 18: 100363.
137. Liu C, Zeng Q, Zhao Y, Yu Y, Yang M, Gao H, et al. Surface ligands management for efficient $CsPbBrI_2$ perovskite nanocrystal solar cells. Solar RRL. 2020; 4: 2000102.
138. Yang J, Siempelkamp BD, Liu D, Kelly TL. Investigation of $CH_3NH_3PbI_3$ degradation rates and mechanisms in controlled humidity environments using in situ techniques. ACS Nano. 2015; 9: 1955-1963.
139. Yoon SJ, Draguta S, Manser JS, Sharia O, Schneider WF, Kuno M, et al. Tracking iodide and bromide ion segregation in mixed halide lead perovskites during photoirradiation. ACS Energy Lett. 2016; 1: 290-296.
140. Liang PW, Liao CY, Chueh CC, Zuo F, Williams ST, Xin XK, et al. Additive enhanced crystallization of solution-processed perovskite for highly efficient planar-heterojunction solar cells. Adv Mater. 2014; 26: 3748-3754.
141. Baloch AAB, Alharbi FH, Grancini G, Hossain MI, Nazeeruddin MK, Tabet N. Analysis of photocarrier dynamics at interfaces in perovskite solar cells by time-resolved photoluminescence. J Phys Chem C. 2018; 122: 26805-26815.
142. Son DY, Lee JW, Choi YJ, Jang IH, Lee S, Yoo PJ, et al. Self-formed grain boundary healing layer

for highly efficient $CH_3NH_3PbI_3$ perovskite solar cells. Nat Energy. 2016; 1: 16081.
143. Handa T, Tex DM, Shimazaki A, Wakamiya A, Kanemitsu Y. Charge injection mechanism at heterointerfaces in $CH_3NH_3PbI_3$ perovskite solar cells revealed by simultaneous time-resolved photoluminescence and photocurrent measurements. J Phys Chem Lett. 2017; 8: 954-960.
144. Eperon GE, Stranks SD, Menelaou C, Johnston MB, Herz LM, Snaith HJ. Formamidinium lead trihalide: A broadly tunable perovskite for efficient planar heterojunction solar cells. Energy Environ Sci. 2014; 7: 982-988.
145. Wang H, Yang F, Li N, Kamarudin MA, Qu J, Song J, et al. Efficient surface passivation and electron transport enable low temperature-processed inverted perovskite solar cells with efficiency over 20%. ACS Sustain Chem Eng. 2020; 8: 8848-8856.
146. Hoke ET, Slotcavage DJ, Dohner ER, Bowring AR, Karunadasa HI, McGehee MD. Reversible photo-induced trap formation in mixed-halide hybrid perovskites for photovoltaics. Chem Sci. 2015; 6: 613-617.
147. Slotcavage DJ, Karunadasa HI, McGehee MD. Light-induced phase segregation in halide-perovskite absorbers. ACS Energy Lett. 2016; 1: 1199-1205.
148. Jacobsson TJ, Correa-Baena JP, Pazoki M, Saliba M, Schenk K, Grätzel M, et al. Exploration of the compositional space for mixed lead halogen perovskites for high efficiency solar cells. Energy Environ Sci. 2016; 9: 1706-1724.
149. Barker AJ, Sadhanala A, Deschler F, Gandini M, Senanayak SP, Pearce PM, et al. Defect-assisted photoinduced halide segregation in mixed-halide perovskite thin films. ACS Energy Lett. 2017; 2: 1416-1424.
150. DeQuilettes DW, Zhang W, Burlakov VM, Graham DJ, Leijtens T, Osherov A, et al. Photo-induced halide redistribution in organic–inorganic perovskite films. Nat Commun. 2016; 7: 1-9.
151. Ahmed GH, El-Demellawi JK, Yin J, Pan J, Velusamy DB, Hedhili MN, et al. Giant photoluminescence enhancement in $CsPbCl_3$ perovskite nanocrystals by simultaneous dual-surface passivation. ACS Energy Lett. 2018; 3: 2301-2307.
152. Kim SG, Chen J, Seo JY, Kang DH, Park NG. Rear-surface passivation by melaminium iodide additive for stable and hysteresis-less perovskite solar cells. ACS Appl Mater Interfaces. 2018; 10: 25372-25383.
153. Noel NK, Abate A, Stranks SD, Parrott ES, Burlakov VM, Goriely A, et al. Enhanced photoluminescence and solar cell performance via lewis base passivation of organic–inorganic lead halide perovskites. ACS Nano. 2014; 8: 9815-9821.
154. Zhao C, Chen B, Qiao X, Luan L, Lu K, Hu B. Revealing underlying processes involved in light soaking effects and hysteresis phenomena in perovskite solar cells. Adv Energy Mater. 2015; 5: 1500279.
155. Shao S, Abdu-Aguye M, Qiu L, Lai LH, Liu J, Adjokatse S, et al. Elimination of the light soaking effect and performance enhancement in perovskite solar cells using a fullerene derivative. Energy Environ Sci. 2016; 9: 2444-2452.
156. Soufiani AM, Hameiri Z, Meyer S, Lim S, Tayebjee MJY, Yun JS, et al. Lessons learnt from spatially resolved electro- and photoluminescence imaging: Interfacial delamination in $CH_3NH_3PbI_3$ planar perovskite solar cells upon illumination. Adv Energy Mater. 2017; 7: 1602111.
157. Chen S, Wen X, Huang S, Huang F, Cheng YB, Green M, et al. Light illumination induced photoluminescence enhancement and quenching in lead halide perovskite. Solar RRL. 2017; 1: 1600001.

158. Deng X, Wen X, Zheng J, Young T, Lau CFJ, Kim J, et al. Dynamic study of the light soaking effect on perovskite solar cells by in-situ photoluminescence microscopy. Nano Energy. 2018; 46: 356-364.
159. Kim GY, Senocrate A, Yang TY, Gregori G, Grätzel M, Maier J. Large tunable photoeffect on ion conduction in halide perovskites and implications for photodecomposition. Nat Mater. 2018; 17: 445-449.
160. Colella S, Todaro M, Masi S, Listorti A, Altamura D, Caliandro R, et al. Light-induced formation of pb^{3+} paramagnetic species in lead halide perovskites. ACS Energy Lett. 2018; 3: 1840-1847.
161. Mora-Sero I, Garcia-Belmonte G, Boix PP, Vazquez MA, Bisquert J. Impedance spectroscopy characterisation of highly efficient silicon solar cells under different light illumination intensities. Energy Environ Sci. 2009; 2: 678-686.
162. Bisquert J. Theory of the impedance of electron diffusion and recombination in a thin layer. J Phys Chem B. 2002; 106: 325-333.
163. Bisquert J, Palomares E, Quiñones CA. Effect of energy disorder in interfacial kinetics of dye-sensitized solar cells with organic hole transport material. J Phys Chem B. 2006; 110: 19406-19411.
164. Mora-Seró I, Luo Y, Garcia-Belmonte G, Bisquert J, Muñoz D, Voz C, et al. Recombination rates in heterojunction silicon solar cells analyzed by impedance spectroscopy at forward bias and under illumination. Sol Energy Mater Sol Cells. 2008; 92: 505-509.
165. Zarazua I, Han G, Boix PP, Mhaisalkar S, Fabregat-Santiago F, Mora-Seró I, et al. Surface recombination and collection efficiency in perovskite solar cells from impedance analysis. J Phys Chem Lett. 2016; 7: 5105-5113.
166. Aranda C, Bisquert J, Guerrero A. Impedance spectroscopy of perovskite/contact interface: Beneficial chemical reactivity effect. J Chem Phys. 2019; 151: 124201.
167. Xie Y, Yin J, Zheng J, Fan Y, Wu J, Zhang X. Facile RbBr interface modification improves perovskite solar cell efficiency. Mater Today Chem. 2019; 14: 100179.
168. Ghahremanirad E, Bou A, Olyaee S, Bisquert J. Inductive loop in the impedance response of perovskite solar cells explained by surface polarization model. J Phys Chem Lett. 2017; 8: 1402-1406.
169. Solanki A, Guerrero A, Zhang Q, Bisquert J, Sum TC. Interfacial mechanism for efficient resistive switching in ruddlesden–popper perovskites for non-volatile memories. J Phys Chem Lett. 2020; 11: 463-470.
170. Wang H, Guerrero A, Bou A, Al-Mayouf AM, Bisquert J. Kinetic and material properties of interfaces governing slow response and long timescale phenomena in perovskite solar cells. Energy Environ Sci. 2019; 12: 2054-2079.
171. Correa-Baena JP, Turren-Cruz SH, Tress W, Hagfeldt A, Aranda C, Shooshtari L, et al. Changes from bulk to surface recombination mechanisms between pristine and cycled perovskite solar cells. ACS Energy Lett. 2017; 2: 681-688.
172. Quere B, Pydzińska-Białek K, Karolczak J, Nowaczyk G, Coy E, Ziółek M. Understanding the effect of different synthesis conditions on the physicochemical properties of mixed-ion perovskite solar cells. Chem Eur J. 2019; 25: 5978-5986.
173. Sun H, Deng K, Xiong J, Li L. Graded bandgap perovskite with intrinsic n–p homojunction expands photon harvesting range and enables all transport layer-free perovskite solar cells. Adv Energy Mater. 2020; 10: 1903347.

174. Cheng H, Li Y, Zhang M, Zhao K, Wang ZS. Self-assembled ionic liquid for highly efficient electron transport layer-free perovskite solar cells. ChemSusChem. 2020; 13: 2779-2785.
175. Zhou L, Guo X, Lin Z, Ma J, Su J, Hu Z, et al. Interface engineering of low temperature processed all-inorganic $CsPbI_2Br$ perovskite solar cells toward pce exceeding 14%. Nano Energy. 2019; 60: 583-590.
176. Bhandari S, Roy A, Ghosh A, Mallick TK, Sundaram S. Perceiving the temperature coefficients of carbon-based perovskite solar cells. Sustain Energy Fuels. 2020; 4: 6283-6298.
177. Wu Y, Chen C, Wang H, Bi W, Song Z, Chen X, et al. Toward ultra-thin and full functional perovskite solar cells by broadband light scattering management and efficient interfacial modification. Sol Energy Mater Sol Cells. 2020; 206: 110297.
178. Xu H, Sun Y, Zheng H, Liu G, Xu X, Xu S, et al. High-performance and moisture-stable perovskite solar cells with a 2D modified layer via introducing a high dipole moment cation. J Mater Chem C. 2019; 7: 15276-15284.
179. Yang Y, Liu Z, Ng WK, Zhang L, Zhang H, Meng X, et al. An ultrathin ferroelectric perovskite oxide layer for high-performance hole transport material free carbon based halide perovskite solar cells. Adv Funct Mater. 2019; 29: 1806506.
180. Li B, Xiang Y, Jayawardena KDGI, Luo D, Wang Z, Yang X, et al. Reduced bilateral recombination by functional molecular interface engineering for efficient inverted perovskite solar cells. Nano Energy. 2020; 78: 105249.
181. Wang G, Dong W, Gurung A, Chen K, Wu F, He Q, et al. Improving photovoltaic performance of carbon-based $CsPbBr_3$ perovskite solar cells by interfacial engineering using P3HT interlayer. J Power Sources. 2019; 432: 48-54.
182. Zhu L, Chen C, Li F, Shen Z, Weng Y, Huang Q, et al. Enhancing the efficiency and stability of perovskite solar cells by incorporating Cds and $Cd(SCN_2H_4)_2Cl_2$ into the $CH_3NH_3PbI_3$ active layer. J Mater Chem A. 2019; 7: 1124-1137.
183. Tavakoli MM, Yadav P, Prochowicz D, Sponseller M, Osherov A, Bulović V, et al. Controllable perovskite crystallization via antisolvent technique using chloride additives for highly efficient planar perovskite solar cells. Adv Energy Mater. 2019; 9: 1803587.
184. Liu Z, Wang L, Xie X. Improving the performance of inverted two-dimensional perovskite solar cells by adding an anti-solvent into the perovskite precursor. J Mater Chem C. 2020; 8: 11882-11889.
185. Liu G, Liu Z, Zeng F, Wang X, Li S, Xie X. High performance two-dimensional perovskite solar cells based on solvent induced morphology control of perovskite layers. Chem Phys Lett. 2020; 743: 137186.
186. Jiang X, Zhang J, Ahmad S, Tu D, Liu X, Jia G, et al. Dion-Jacobson 2D-3D perovskite solar cells with improved efficiency and stability. Nano Energy. 2020; 75: 104892.
187. Green MA, Dunlop ED, Hohl-Ebinger J, Yoshita M, Kopidakis N, Hao X. Solar cell efficiency tables (version 56). Prog Photovoltaics Res Appl. 2020; 28: 629-638.
188. Stolterfoht M, Caprioglio P, Wolff CM, Márquez JA, Nordmann J, Zhang S, et al. The impact of energy alignment and interfacial recombination on the internal and external open-circuit voltage of perovskite solar cells. Energy Environ Sci. 2019; 12: 2778-2788.
189. Shockley W, Read WT. Statistics of the recombinations of holes and electrons. Phys Rev. 1952; 87: 835-842.
190. Hall RN. Electron-hole recombination in germanium. Phys Rev. 1952; 87: 387.

191. Singh T, Ikegami M, Miyasaka T. Ambient fabrication of 126 µm thick complete perovskite photovoltaic device for high flexibility and performance. ACS Appl Energy Mater. 2018; 1: 6741-6747.
192. Kim HS, Jang IH, Ahn N, Choi M, Guerrero A, Bisquert J, et al. Control of I–V hysteresis in $CH_3NH_3PbI_3$ perovskite solar cell. J Phys Chem Lett. 2015; 6: 4633-4639.
193. Chen HW, Sakai N, Ikegami M, Miyasaka T. Emergence of hysteresis and transient ferroelectric response in organo-lead halide perovskite solar cells. J Phys Chem Lett. 2015; 6: 164-169.
194. Calado P, Telford AM, Bryant D, Li X, Nelson J, O'Regan BC, et al. Evidence for ion migration in hybrid perovskite solar cells with minimal hysteresis. Nat Commun. 2016; 7: 1-10.
195. Unger EL, Hoke ET, Bailie CD, Nguyen WH, Bowring AR, Heumüller T, et al. Hysteresis and transient behavior in current–voltage measurements of hybrid-perovskite absorber solar cells. Energy Environ Sci. 2014; 7: 3690-3698.
196. Sanchez RS, Gonzalez-Pedro V, Lee JW, Park NG, Kang YS, Mora-Sero I, et al. Slow dynamic processes in lead halide perovskite solar cells. Characteristic times and hysteresis. J Phys Chem Lett. 2014; 5: 2357-2363.
197. Kim HS, Kim SK, Kim BJ, Shin KS, Gupta MK, Jung HS, et al. Ferroelectric polarization in $CH_3NH_3PbI_3$ perovskite. J Phys Chem Lett. 2015; 6: 1729-1735.
198. Boyd CC, Cheacharoen R, Leijtens T, McGehee MD. Understanding degradation mechanisms and improving stability of perovskite photovoltaics. Chem Rev. 2019; 119: 3418-3451.
199. Li W, Zhang W, Reenen SV, Sutton RJ, Fan J, Haghighirad AA, et al. Enhanced UV-light stability of planar heterojunction perovskite solar cells with caesium bromide interface modification. Energy Environ Sci. 2016; 9: 490.
200. Khenkin MV, Katz EA, Abate A, Bardizza G, Berry JJ, Brabec C, et al. Consensus statement for stability assessment and reporting for perovskite photovoltaics based on isos procedures. Nat Energy. 2020; 5: 35-49.
201. Saliba M, Stolterfoht M, Wolff CM, Neher D, Abate A. Measuring aging stability of perovskite solar cells. Joule. 2018; 2: 1019-1024.
202. Ghosh S, Singh T. Long term stability assessment of perovskite solar cell via recycling of metal contacts under ambient conditions. Mater Lett. 2022; 322: 132490.
203. Rakocevic L, Ernst F, Yimga NT, Vashishtha S, Aernouts T, Heumueller T, et al. Reliable performance comparison of perovskite solar cells using optimized maximum power point tracking. Solar RRL. 2019; 3: 1800287.
204. Köbler H, Neubert S, Jankovec M, Glažar B, Haase M, Hilbert C, et al. High-throughput aging system for parallel maximum power point tracking of perovskite solar cells. Energy Technol. 2022; 10: 2200234.
205. Tao L, Qiu J, Sun B, Wang X, Ran X, Song L, et al. Stability of mixed-halide wide bandgap perovskite solar cells: Strategies and progress. J Energy Chem. 2021; 61: 395-415.
206. Yang TCJ, Fiala P, Jeangros Q, Ballif C. High-bandgap perovskite materials for multijunction solar cells. Joule. 2018; 2: 1421-1436.
207. Song Z, Chen C, Li C, Awni RA, Zhao D, Yan Y. Wide-bandgap, low-bandgap, and tandem perovskite solar cells. Semicond Sci Technol. 2019; 34: 093001.

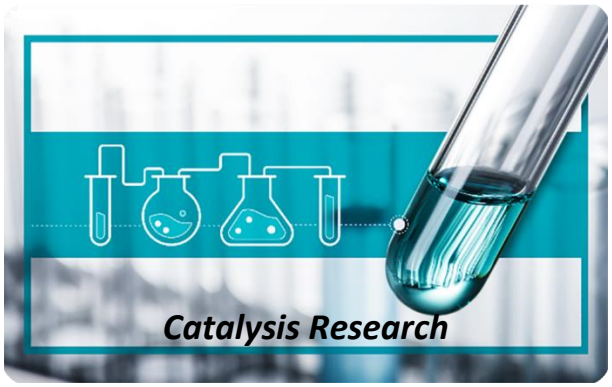

Enjoy *Catalysis Research* by:

1. Submitting a manuscript
2. Joining in volunteer reviewer bank
3. Joining Editorial Board
4. Guest editing a special issue

For more details, please visit:
http://www.lidsen.com/journals/cr